Final Report

Project Number:

DOE-EE0007753

Recipient:

Daikin America

Project Title:

Daikin Advanced Lithium Ion Battery Technology – High Voltage Electrolyte

Project Director/Principal Investigator:

Ron Hendershot, Joseph Sunstrom, Alec Falzone

Team Members:

Chad Meserole
Michael Gilmore
Abundio Sandoval
Arsela Haque
Ferdousi Khan
Ana Pacheco
Emily Grumbles
Natalia McMahon
Melissa Costa
Megan Flannigan
Michael Kurzban
Teresa Stewart

Collaborators

Dr. Julia Chan (University of Texas – Dallas)
Physical Electronics, USA

Executive Summary

An evaluation of high voltage electrolytes which contain fluorochemicals as either co-solvents or additives has been completed. The project objective was to identify a cell chemistry and electrolyte formulation which is capable of operating at 4.6 V. Stable cycle performance has been demonstrated in $LiNi_{0.50}Mn_{0.30}Co_{0.20}O_2$ (NMC532)/Artificial Graphite pouch cells to 4.6 V, with a discharge capacity retention greater than 80% after 300 cycles. A multitude of physical and chemical changes between 4.2 and 4.6V were investigated, with the goal of correlating identified degradation mechanisms with premature cell failure.

Milestone	Type	Description	Status
Establish Baseline and Review Current State of the Art	Technical	Compile baseline electrochemical and physical property specifications for current best practice electrolyte	Completed
Gas Composition	Technical	Assemble plots of gas product concentrations as a function of performance parameters	Completed
Gassing Kinetics of FEC	Technical	Assemble plots of gas volume and FEC concentration as a function of performance parameters (voltage, initial capacity, cycle #) to understand gassing due to FEC.	Completed
Gassing Kinetics Based on Cathode Surface Composition	Go/No-Go	Assemble plots of gas volume and gas product concentrations as a function of performance parameters (voltage, initial capacity, cycle #) to understand effects of surface chemistry on performance	Completed
Film Thickness vs. Time/Voltage	Technical	Assemble plots of film thickness as a function of performance parameters (voltage, initial capacity, cycle #) to understand effects of film thickness on performance	Completed
Film Composition (Elemental) vs. Time/Voltage	Technical	Assemble plots of film composition (elemental) as a function of performance parameters (voltage, initial capacity, cycle #) to understand effects of film composition on performance.	Completed
Battery Thickness (non-gas) vs. Time/Voltage	Technical	Assemble plots of cell thickness as a function of performance parameters (voltage, initial capacity, cycle #) to understand what effects cell swelling has on performance.	Completed
Interim Cells Achieve a Significant	Go/No-Go	Interim cells achieve a significant improvement over initial cells submitted at the beginning of the project when cycled at 4.6V.	Completed

Improvement in Cycling at 4.6V			
Metal Dissolution vs. Time/Voltage	Technical	Assemble plots of transition metal concentration as a function of performance parameters (voltage, initial capacity, cycle #) to understand what effects cathode dissolution has on cell performance.	Completed
Cathode Surface Structure vs. Time/Voltage	Technical	Assemble plots of crystalline impurities as a function of performance parameters (voltage, initial capacity, cycle #) to understand what effects structural changes in the cathode have on performance	Completed
Compilation of Performance Data and Selection of New Electrolyte Composition	Technical	Data analysis of results compiled throughout the project to understand correlations between electrochemical performance and hypothesized failure mechanisms	Completed
Submit Final Cells and Report to the DOE	Technical	Final cells to target at least 300 cycles at 4.6V	Achieved

Introduction

Electrification of vehicles has accelerated immensely over the past decade, with many recent announcements of increased investment and commitment to the transition to all things related to electric vehicles (EV). This has resulted in significant advances in a variety of energy storage technologies, with many focused on next-generation lithium ion batteries. Not only are lithium ion batteries of great importance in mobility, but increased reliance on portable consumer electronics and grid storage using these technologies are evident. To meet the evolving demands in these technology areas, it is necessary to develop cell design solutions which both increase the useable lifetime of the battery and increase the energy density of each individual cell. To achieve these demanding performance metrics, there are a few different routes to purse. 1) Implement higher capacity active materials such as silicon or lithium metal anodes in combination with high-Nickel cathodes such as NMC811. 2) Improve the cell design through thinner current collectors, thicker electrode coatings, using a more durable gasket material in cylindrical cells, and using a more efficient cell geometry. 3) Increase the energy density of the cell by operating at a higher voltage. Commonly used electrolyte formulations, such as the Gen 2 electrolyte (1.2M Lithium Hexafluorophosphate ($LiPF_6$) Ethyl Methyl Carbonate (EMC) 70%, Ethylene Carbonate (EC) 30%) are not stable at these high voltages due to their susceptibility to electrochemical oxidation. One approach to achieve a higher operating voltage (> 4.3V) is to introduce fluorinated additives and co-solvents to stabilize the liquid electrolyte at these increased potentials. These fluorinated

electrolytes take advantage of the extreme electronegativity of Fluorine and chemical stability of the Carbon-Fluorine bond. Developing an optimized electrolyte formulation for use with NMC cathodes using small fluorinated molecules to increase the energy density of lithium ion batteries is the focus of this project. This study also aims to develop an understanding of observed failure mechanisms at high voltage such as gas generation and swelling. Another aim is to probe surface chemistry effects and solid-state structural changes seen with fluorinated electrolytes.

Daikin has previously shown that it is possible to operate lithium ion batteries utilizing several different cathode chemistries up to 4.5 V.[1] This is accomplished by reducing the gas generation originating from electrolyte decomposition at high voltage. The primary mechanism for this is not completely understood, but one hypothesis is that the fluorinated molecules within the electrolyte form a protective film on the highly oxidizing cathode. This layer is sometimes referred to as the Cathode-Electrolyte-Interface, or CEI layer. It is known that cycle life performance above 4.5 V degrades significantly; but the source of the observed performance loss is not yet understood. **Figure 1** depicts preliminary Auger Electron Spectroscopy (AES) data obtained prior to the start of this project, suggesting the presence of a highly fluorinated film on the surface of the cathode. This data was obtained through analyzing the cathode post-cycle life testing, supporting the notion that this CEI layer is formed as a result of the fluorinated electrolyte interacting with the highly oxidizing surface of the cathode at high voltage. In order to investigate effects of this cathode surface chemistry as a function of electrolyte formulation and voltage, a combination of different surface analysis techniques is employed to probe these characteristics.

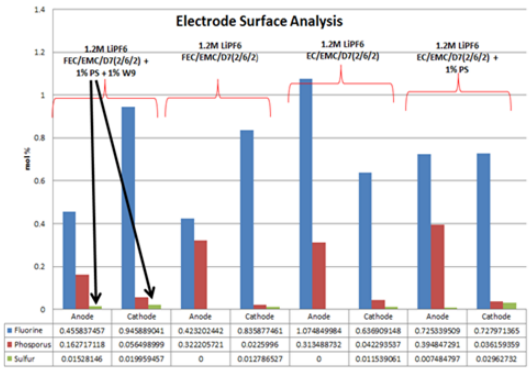

	Anode	Cathode	Anode	Cathode	Anode	Cathode	Anode	Cathode
Fluorine	0.455837457	0.945889041	0.423202442	0.835877461	1.074849984	0.636909148	0.725339509	0.727971365
Phosporus	0.162717118	0.056498999	0.322205721	0.0225996	0.313488732	0.042293537	0.394847291	0.036159359
Sulfur	0.01528146	0.019959457	0	0.012786527	0	0.011539061	0.007484797	0.02962732

Figure 1: AES data obtained in a previous project (DOE EE0006437) on NMC111 cathodes with fluorinated electrolyte revealed a high concentration of Fluorine on the cathode surface. A proposed function of this increased fluorine concentration is the CEI layer, and originating from the fluorinated electrolyte.

The electrochemical performance target for this project is to achieve at least 300 cycles at 4.6V, with at least 80% discharge capacity retention. A better understanding of observed gas evolution, which happens above 4.3 V, and the failure mode above 4.5 V, is sought in order to propose mitigation strategies which will facilitate better high voltage performance in lithium ion batteries. Gas chromatography in combination with a mass spectrometer (GC-MS) is a widely utilized analytical technique to understand the chemical composition of gas generated in lithium ion batteries, along with quantifying how much is present. One of the major contributors to gassing in lithium ion batteries, especially at high voltage, is fluoroethylene carbonate (FEC). This observation has been well reported in the literature, outlining different methodologies to extract

and analyze gas from lithium ion batteries.[2-8] Kinetic studies of the rate of gas generation as a function of FEC concentration with cells at 100% SOC will be performed at different elevated temperatures to gain insight into this observation. A method has been developed to extract, separate, identify, and quantitate gas generated in pouch cells. **Figure 2** shows a representative chromatogram of gases identified following a calendar life test at an elevated temperature. Representative data was obtained from an NMC811 pouch cell with a fluorinated electrolyte. Qualitative and quantitative analysis of gases extracted from lithium ion batteries will be one of the primary focuses of this work.

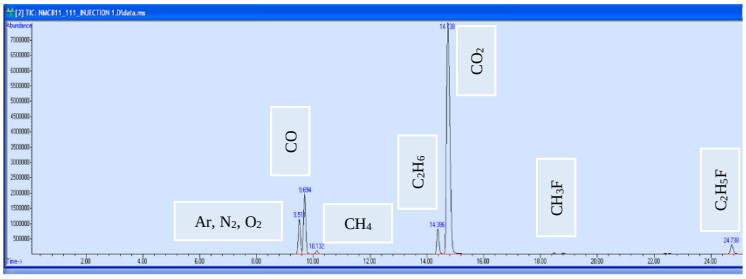

Figure 2: Representative gas chromatogram identifying typical components present in a lithium ion battery which has gassed at high voltage. CO_2 is the main component, with various hydrocarbons and fluorocarbons making up the rest of the gas.

The battery industry trend for implementing new cathode materials is geared towards reducing the Cobalt content (i.e. higher Nickel) for a variety of reasons. Some of which include: increasing market price of Cobalt, increased risk of not securing enough supply for production, and human rights concerns observed in the mining process.[9] NMC811 is the current leading candidate as a cathode material for EV's, whereas just a few years ago NMC111 was the most widely utilized material. Thus the identified trend of moving towards reducing Cobalt content in the cathode has held true since the commencement of this project. Additional efforts proposed for this project will encompass a range of cathode materials with successively higher nickel content in order to understand how fluorinated electrolyte interacts with various cathode surfaces. This is with the anticipation that the lithium ion battery industry will continue its move towards a cathode with an even higher nickel content (i.e. 90+%). The assumption is that an even higher Ni content can operate at higher voltages to achieve more energy-dense batteries.

Changes to the bulk crystal structure of the cathode are expected, especially at high voltage. Many novel approaches to probing these changes have been reported,[10-14] however an increased understanding of observed changes above 4.5V is needed. In addition, the project aims to investigate any influences fluorinated electrolytes may have on mitigating cathode degradation (oxygen evolution and/or transition metal dissolution), or reducing any observed swelling of the jelly roll at high voltage. Powder X-ray diffraction (XRD) and inductively coupled plasma mass spectrometry (ICP-MS) are techniques implemented to probe these changes in cathode crystallinity and quantify dissolved transition metals. Baseline diffraction patterns of the layered structures of cathodes used throughout the project can be seen in **Figure 3**. These dissolved transition metals (Ni, Mn, and Co) either end up deposited at the anode, or remain solvated by the electrolyte and in solution. Along with changes to the cathode crystalline structure, this deposition of dissolved transition metals at the anode is just one of the contributing phenomena to observed swelling of

solid components in the battery. These thickness changes are not related to the previously discussed gas generation, which also swells the pouch cell. The major contributing factor to this observed thickness increase is the entrapment of intercalated lithium within the graphite lattice and continuous SEI layer growth, which also manifests itself with irreversible capacity loss.[15] An instrumental setup has been designed, and a method developed to study these thickness changes in real-time through multiple charge/discharge cycles.

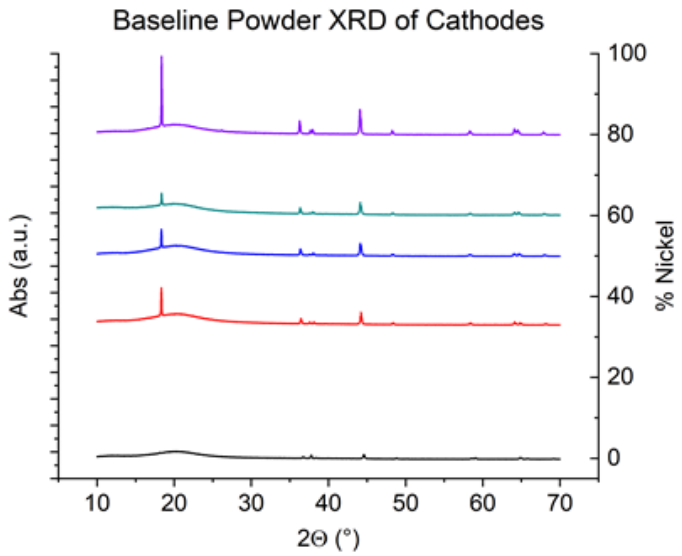

Figure 3: Powder X-ray diffraction patterns for LCO and all NMC cathodes used throughout the project. Baseline powder diffraction patterns were obtained from dry cells prior to any testing. Data is ordered as a function of Ni concentration (mol %) within the cathode: LCO (**black**), NMC111 (**red**), NMC532 (**blue**), NMC622 (**teal**), and NMC811 (**violet**) are depicted.

In summary, the four-year project (FY2017-FY2020) can be categorized into three main milestone areas: 1) understanding of gassing mechanisms and kinetics, 2) examining physical and chemical aspects of film formation, and 3) observation of chemical and structural evolution of electrode surfaces at various operating conditions. To benchmark the electrochemical performance of the project, interim cells were delivered in FY2019 to the Department of Energy (DOE) to be tested at a 3rd party facility for cycle life testing. Cells with the project's baseline hydrocarbon electrolyte were compared alongside the best-practice fluorinated electrolyte. Electrochemical testing of commercial prismatic pouch cells was performed continuously throughout the project for both the outlined objectives of failure analysis in addition to identifying an optimized electrolyte formulation and cell chemistry to meet the overall project objective (A minimum of 300 charge/discharge cycles at 4.6V). At the completion of the project, final cells will be delivered to the Department of Energy (DOE) with the optimized fluorinated electrolyte and cell chemistry for testing to gauge the performance of cells versus the overall proposed performance targets.

Experimental

Pouch Cell Chemistry

Dried and sealed 200 mAh pouch cells of various chemistries were purchased from LiFun (China) through Pred Materials. $LiCoO_2$ (LCO), $LiNi_{0.33}Mn_{0.33}Co_{0.33}O_2$ (NMC111),

$LiNi_{0.50}Mn_{0.30}Co_{0.20}O_2$ (NMC532), $LiNi_{0.60}Mn_{0.20}Co_{0.20}O_2$ (NMC622), $LiNi_{0.80}Mn_{0.10}Co_{0.10}O_2$ (NMC811), and $LiNi_{0.85}Co_{0.10}Al_{0.05}O_2$ (NCA) were all paired with artificial graphite (AG) anodes in a wound prismatic cell geometry. Since different upper cutoff voltages were utilized throughout the project, all cells purchased were balanced at the median potential at a 4.4V operating voltage.

Electrolyte Preparation

Battery grade Lithium Hexafluorophosphate ($LiPF_6$) salt was the only salt used throughout the project, and was purchased from Kanto Denka (Japan). All carbonate components of the electrolyte were of battery grade purity and used as received unless otherwise noted. Ethylene Carbonate (EC), Ethyl Methyl Carbonate (EMC), and Dimethyl Carbonate (DMC) were purchased from Kishida Chemical (Japan). 1,3-Propane Sultone (PS) and Fluoroethylene Carbonate (FEC) were purchased through HighChem America. The fluoroether (HFE) used throughout the project was produced and obtained from Daikin Industries Ltd. (Japan). All solvents and other electrolyte components were stored and used in an Argon-filled glovebox (Innovative Technologies, PureLab HE) which had less than 0.1 ppm H_2O and 1.0 ppm O_2.

Perfluoroalkoxy alkane (PFA) bottles were used to mix electrolyte components inside the glovebox, and dried at 125 °C for at least 24 hours prior to use. To mix the electrolyte, the major liquid components were added to the PFA bottle first (EMC and HFE typically). Followed by either EC or FEC. Once the carbonates and HFE (if used) were thoroughly mixed, the $LiPF_6$ salt was added in four small aliquots to minimize the exotherm. Once the solution had cooled to room temperature the PS additive was added, followed by an additional mixing step. Once prepared, the electrolyte was transferred into an oven dried (125 °C) stainless steel bottle, and sealed with a polytetrafluoroethylene (PTFE) disc.

Cell Building and Formation

Prior to dosing the pouch cells with electrolyte, they were cut open and dried at 60 °C in a vacuum oven for five hours. This vacuum chamber is directly affixed to an Argon-filled glovebox (Inert Technologies, PureLab HE) which had less than 0.1 ppm H_2O and 0.5 ppm O_2. Cells were transferred to the glovebox, and each pouch cell was dosed volumetrically (1.0 mL) with electrolyte using an analytical micropipette. These were then placed in the vacuum oven under reduced pressure for 5 minutes, then brought back to atmospheric pressure under Argon. They were let rest for 55 additional minutes prior to sealing with a heated vacuum sealer (Fuji Impulse FCB-200) in an Argon-filled glovebag. The weight of each cell after vacuum sealing was recorded to determine the amount of electrolyte in each cell. After sealing, the cells were connected to a channel unclamped using alligator clips (Arbin Instruments or Kikusui) and let rest for 8 hours. Cells were formed between 3.0V and the upper cutoff voltage (4.2, 4.5, or 4.6V) for two charge/discharge cycles at C/20, followed by a final CC-CV prior to additional testing. Initial cell volumes were recorded both before and after formation using the Archimedes method (Qualitest MD300-S Densimeter) in an ethanol media (Reagent Alcohol, Sigma Aldrich) which was used as received.

Elevated Temperature Calendar Life Testing, Gas Extraction and Quantification

Calendar life testing was performed at 35, 45, and 55 °C in an enclosed environmental chamber (Espec BTU-133). Volume measurements of the cells were taken to study gassing kinetics using the Archimedes method previously described. OCV measurements were recorded using the same time increments as the volume measurements using a digital multimeter (AmProbe AM-60).

Manually extracting battery gas with a syringe from pouch cells has the potential to cause excess atmospheric contamination during injections. A two-layer coating was applied to the external of the pouch cells to act as a self-sealing mechanism around the needle to minimize this backflow contamination of air. Pouch cells used for gas quantification via GC-MS were coated in two sequential steps. To establish a more adhesive substrate for the final rubberized coating, batteries were initially coated with a thin layer of Weldwood® Contact Cement (DAP Products, Inc.) and hung freely to dry in a fumehood. The pouch cells were then submerged in Plasti Dip® (Plasti Dip International) and hung to dry overnight. All injections were obtained using the same injection site from where the initial injection occurred to demonstrate the repeatability of this method compared to the uncoated analog. No residual solvent contaminates were detected by the MSD from the coating process (i.e. Xylenes), supporting the notion an overnight cure time is required.

No batteries in this study were known to produce N_2, the major component of air (78%), so any amount of N_2 detected via GC-MS was correlated to atmospheric contamination, and not originating from the battery itself. The parent m/z peak of 28 amu for N_2 was used for quantification purposes, with the primary fragment of 14 amu for additional accuracy. A gastight Hamilton blunt-tip syringe was retrofitted with a Hamilton Chaney Adaptor and used to extract 200 μL of gas from the pouch cells. The GC-MSD used was an Agilent Technologies 6890N GC system with a split injector (120 °C, 35:1 ratio) with a liquid nitrogen cryogenic valve (Agilent) and a corresponding 50L liquid nitrogen dewar. A silica capillary column (Agilent GasPro, 60m, 0.32 mm ID, 0 μm coating) was used to elute the light hydrocarbons and permanent gases including CO_2. Helium (Airgas, 99.999%) was used as the carrier gas with a flow rate of 1.5 mL/min. The injected gas was met with an initial oven temperature of -10 °C for 5 minutes, a first ramp of 20 °C/min to 110 °C, a second ramp of 20 °C/150 °C, and a post-run temperature held for 5 minutes at 180 °C. Reported values are the average of three injections from at least two batteries within a data set. Concentrations were determined by comparison to calibration curves generated from custom gas mixtures.

Gas Mixing Manifold and GC-MS Calibration Standards

To produce the calibration curve for quantitation, the custom gas manifold system was supplied with Ultra High Purity CH_3F (99.0%), C_2H_5F (99.0%), CHF_3 (98.0%) (Synquest Laboratories) CH_4 (99.999%), C_2H_4, CO (99.999%), CO_2 (99.99%), H_2 (99.999%) (Airgas), C_2H_6 (99.95%), O_2 (99.99%) (Mesa Gas), and He (99.999%) balancing gas (Airgas). Stainless steel fittings to control gas flow were purchased from Swagelok and assembled accordingly. Stainless steel transport cylinders (Restek, 75cc) were made using Swagelok fittings to house the custom mixed gases for GC-MS injection. Partial pressures were used to equate to percentages of individual gas needed with an Omega DPG4000 Series digital pressure gauge (± 0.10% accuracy).

Surface/Material Analysis – Auger Electron Spectroscopy (AES), X-ray Photoelectron Spectroscopy, Focused Ion Beam/Scanning Electron Microscopy (FIB-SEM), and Time-of-Flight Secondary Ion Mass Spectrometry (TOF-SIMS)

Cells analyzed using various surface analytical techniques were first deconstructed in an Ar-filled glovebox (Inert Technologies, PureLab HE). To safely perform this, pouch cells were cut using non-conductive ceramic scissors to avoid short-circuiting. The jelly roll was pulled apart using plastic tweezers with the cathode and anode electrodes isolated and placed in separate containers for storage. To avoid the possible dissolution of any polymeric CEI layer on the cathode, samples were not rinsed with any solvent prior to analysis.

For AES analysis and depth profiling a 1 x 1 cm portion of cathode was cut from the electrode using ceramic scissors and left open inside the glovebox to allow any remaining liquid electrolyte to evaporate. The cathode was loaded onto a 1" sample puck and transferred into a custom made vacuum transfer suitcase (UHV Transfer Systems, Inc.) for introduction into the AES UHV system (Perkin Elmer – Physical Electronics Division). Cathode samples used in the XPS system (Perkin Elmer – Physical Electronics Division) were prepared and transferred into the analytical chamber using an identical method to that used for AES analysis.

FIB-SEM analyses were performed on the carbon film standards (UHV Sputtering) at a 3rd party testing laboratory. Cross sectional samples were initially sputtered with conductive Platinum layer and prepared normal to the surface in an FEI FIB200 FIB instrument. FIB cuts were performed on the cleaved wafer edge and SEM images taken normal to the analytical surface but parallel to the sample surface. Electron images were true and did not require any adjustments for tilt. Samples were imaged using a Hitachi S-4800 Cold-Field-Emission SEM normal to the analytical surface.

Chemical information of the CEI layer was obtained through performing TOF-SIMS analysis on cathodes from cycled batteries. These experiments were obtained at Physical Electronics USA (ULVAC-PHI) using a PHI *nano*TOF II instrument affixed with a multi-sample plate in the analytical chamber. An Ar_{2500}^{+} gas cluster ion gun was used to lightly sputter the surface of the cathodes prior to analysis. Cathodes for analysis were prepared as previously described for AES and XPS, but were performed in an Ar-filled glovebox at the test lab facility. All cathodes were loaded onto the multi-sample plate and all loaded into the load lock chamber. These were pumped down using the turbo pump overnight to remove any residual liquid electrolyte and adsorbed substances from the surface.

Dissolved Metals Analysis and Powder X-ray Diffraction

Quantification of dissolved metals were obtained through ICP-MS analysis of charged anodes post-mortem. The reported data was obtained by a 3rd party analysis lab (Galbraith Laboratories). Cells were first charged to their upper voltage and carefully deconstructed inside an Ar-filled glovebox (Inert Technologies) using non-conductive ceramic scissors. The ribbons containing the cathode and anode were carefully separated from each other using plastic tweezers and any remaining electrolyte on the active material surfaces were allowed to dry inside the glovebox. To gain a comprehensive understanding of overall dissolved transition metal content in

the cell, 1 cm wide sample portions were cut from the terminals and middle of the anode. Each section was of approximately equal weight and physical dimension. These pieces of graphite anodes were weighed, placed into scintillation vials, and left open to atmosphere inside a fume hood for at least 48 hours prior to analysis. All three sections of anode were acid digested together prior to being injected for analysis.

Preliminary powder X-ray Diffraction (XRD) data on NMC532 cathodes was obtained in collaboration with Dr. Julia Chan (University of Texas at Dallas). Cells were deconstructed under Argon as previously described. Portions of cathode were first rinsed repeatedly with dry DMC to remove any residual liquid electrolyte and crystalline $LiPF_6$. These cathodes were then let dry at atmospheric pressure under Argon prior to analysis. In lieu of using an airtight specimen holder, cathodes were vacuum sealed inside a plastic bag to enable ex-situ analysis and avoiding cathode degradation due to atmospheric exposure.

Additional powder XRD samples were analyzed at a 3rd party materials analysis laboratory. Samples were stored and prepared in a N_2 purge box. All samples were prepared just prior to XRD analysis. These were prepared by placing the entire folded cathode film onto low background mounts which were then sealed used Kapton® film. Samples were removed from the N_2 purge box and analyzed using a Panalytical X'Pert Pro MPD X-ray diffractometer. The samples were scanned over $5° \leq 2\Theta \leq 85°$ using step size = 0.033° and count rate = 400 s/step. Panalytical HighScore+ v4.8 was used to determine the background for each dataset and identify diffraction peaks. Diffraction peaks were then matched to the reference patterns for Li-Ni-Mn-Co-O phases from the ICDD PDF-4+ 2020 database.

Pouch Cell Thickness Change Determination

The initial approach to determine thickness changes in pouch cells versus time while cycling used contact displacement sensors (Keyence Corporation, GT2-H12KL) which were affixed to a custom fabricated aluminum housing. Analog data was recorded through a channel on a battery tester (Arbin Instruments), and thickness versus thickness change calibration curves were generated. The output voltage (14 V) from the analog signal of the sensor was brought within the voltage range of the battery tester by creating a simple circuit with a 180 Ω resistor.

The second approach used to measure thickness changes of pouch cells utilized a pseudo-interferometer method which tracks the reflected laser position to changes in position along the z-axis. This change in the location of the reflection plane, or z-axis, is correlated to swelling of the pouch cell. A reflector (1" x 3" glass microscope slide) is placed on top of the battery at an angle. A CW red laser (LBD-635, LaserGlow) is glanced off the reflector onto a target approximately 5' away. To record the position, a CMOS camera (1280 x 1024 pixels) recorded the location of the spot every 10 seconds, and controlled by ImageJ Micromanager.[16] The Trackmate plugin for Fiji / Image J tracked the laser movement in all images for the experiment, generating a table (x,y) values for the spot position in each frame/image. Prior to initiating the experiment, a calibration curve is generated by manipulating the instrument micrometer to simulate swelling of the battery by a known distance along the z-axis.

Work in the first year (FY2017) was divided into two tasks to accomplish the first four milestones: 1) Establish a baseline based on knowledge gained from first DOE funding opportunity (DOE Project EE0006437) and 2) Initiate setup of instruments and samples for gas analysis. Final cell test results from Argonne National Laboratory were received at the end of March CY2017. Cycle life testing results are shown in **Figure 4** for three groups:

a. Group 1 is a hydrocarbon electrolyte cycled to 4.5 V, (**black**)

b. Group 2 contains a fluorocarbon best practice electrolyte cycled to 4.5 V, (**red**)

c. Group 3 contains the same fluorocarbon as Group 2 but cycled to 4.6 V, (**blue**)

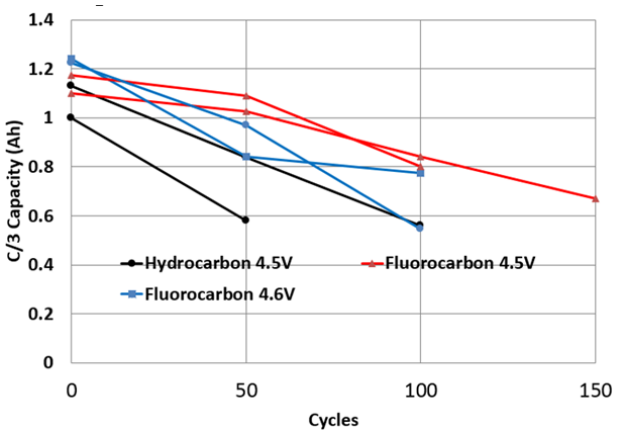

Figure 4: Cycle life (C/3) discharge for a) hydrocarbon electrolyte charged to 4.5 V (black), 2) fluorocarbon electrolyte charged to 4.5 V (red), and fluorocarbon electrolyte charged to 4.6 volt (blue). Cells were 1 Ah wound prismatic pouch cells with a NMC111/Graphite cell chemistry.

These third party test results confirm previous Daikin internal results which indicate that fluorocarbon electrolyte performs better than hydrocarbon up to 4.5 V. However, there is a performance decrease when the upper voltage is extended to 4.6 V, even when using a fluorinated electrolyte. This result adjusted the upper cutoff voltages for the project to 4.2 V where both electrolytes perform, 4.5 V where only the fluorinated analog works, and 4.6 V where the fluorinated electrolyte exhibits significant degradation. Cells reached the failure point of 80% capacity retention around or before 100 cycles at C/3.

Additional baseline experiments were performed in order to adjust experimental parameters to generate gas in a timely manner for analysis. **Figure 5** depicts the volume change in pouches containing NMC111 charged cathodes (delithiated) with graphite anodes (lithiated) stored with electrolyte at 60 °C. The targeted temperature settings following these calendar life tests were established as 35, 45 and 55 °C.

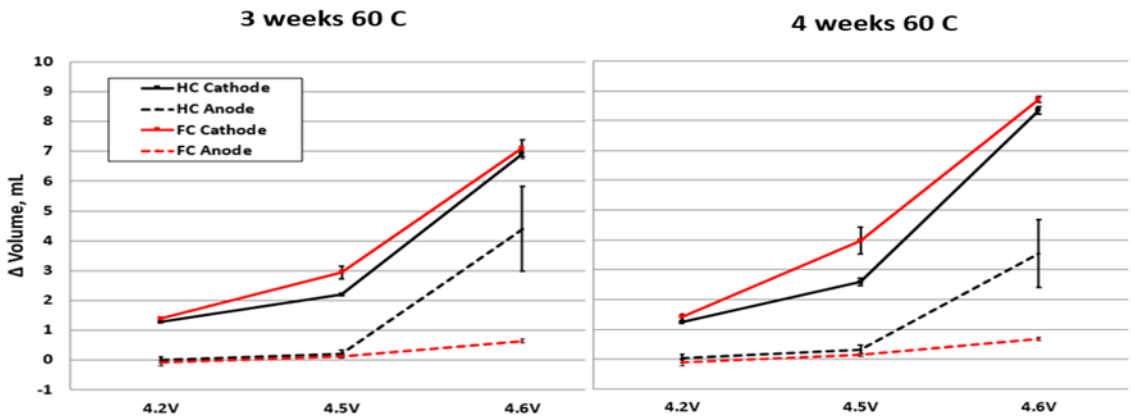

Figure 5: Gas volume change at 3 weeks (left) and 4 weeks (right) for NMC111 cathodes with graphite anodes when exposed to electrolyte at 60 °C

As the charged voltage is increase from 4.2 to 4.6V, an increase in the amount of gas generated at 60 °C is observed. The increase in gas generation seen in the lithiated graphite anodes at 4.5 and 4.6V can be attributed to the reductive decomposition, with FEC being a strong candidate as the source. The charged cathodes generate the largest amount of gas at all voltages, which is likely due to the oxidation of the carbonate components in the electrolyte (EMC, EC, etc.). Future efforts are aimed at qualitatively and quantitatively identifying the components at high voltage (≥4.5V) as a function of cell chemistry and electrolyte formulation. The baseline electrolyte for the project was established as 1.2M $LiPF_6$, 80% EMC, 20% EC (v/v) + 1% PS (w/w) as an anti-gassing additive. Two baseline fluorinated electrolyte formulations were also established, with 1.2M $LiPF_6$, 60% EMC, 20% HFE, 20% FEC (v/v) + 1% PS (w/w) being the totally fluorinated analog and 1.2M $LiPF_6$, 60% EMC, 20% HFE, 20% EC (v/v) + 1% PS (w/w) the partially fluorinated derivative.

Additional efforts in Budget Period 1 were allocated to the expansion of the project's analytical capabilities, number of available battery testing channels, and personnel. Two Co-op Students and a Postdoctoral Research Scientist were hired to meet project objectives. **Figure 6** depicts additional equipment either brought online, or upgraded, throughout the first year of the project. Upgrades to existing gas analysis capabilities enabled both the qualitative and quantitative investigation of gassing in LiB's throughout the project. The installation and commissioning of surface analysis equipment to support technical milestones in future budget periods also occurred early on in the project. Both Auger Electron Spectroscopy (AES) and X-ray Photoelectron Spectroscopy (XPS) enable elemental and chemical analysis of battery component surface composition.

To determine the gas composition as a function of various operating conditions ([FEC], voltage, cathode material, etc.), ninety (LCO, NMC622) 200 mAh cells were constructed for an extended open circuit voltage (OCV) test to be carried out at various temperatures for analysis. These cells underwent initial formation then were charged to constant voltage to the desired voltage (4.2, 4.5, and 4.6 V) and placed into ovens at 35, 45, and 55 °C. Following this extended aging period with intermittent volume measurements, the cells were discharged and punctured with a gas tight syringe for headspace analysis. This initial approach using NMC622 and LCO was

to determine the optimum upper temperature for extended storage at high voltage along with producing a substantial set of pouch cells to help develop the project's gas analysis method. LCO (0% Ni) and NMC622 (60% Ni) represented both the upper and lower limit of Ni in the cathode in commercial available cells at the onset of the project in FY2016.

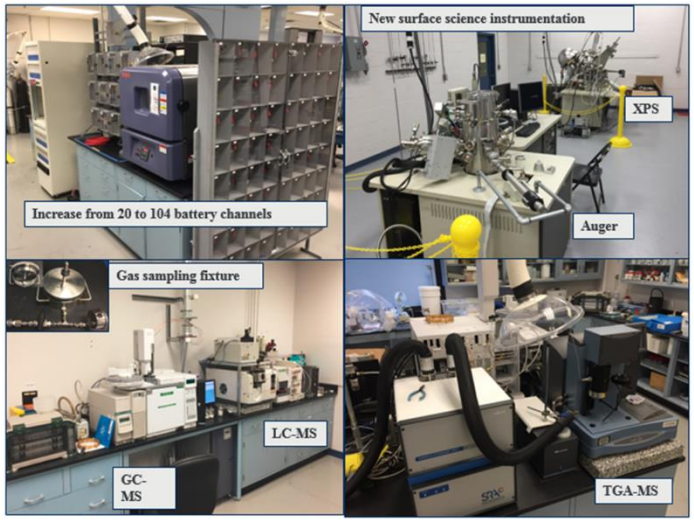

Figure 6: A 64 channel Arbin battery tester and additional channels on the existing Kikisui unit expanded the available channels to 104. Additional upgrades to the GC/MS and thermal analysis instrumentation expanded gas analysis capabilities.

Determination of degradation components through gas analysis was initially performed using GC in combination with both a mass spectrometer (MS) and thermal conductivity (TC) detector. This approach was used to qualitatively identify every possible component in gas mixtures extracted from aged cells. While most components could be identified using the MS, hydrogen (H_2) was not detected due to its low M/W (m/z = 2). All assigned peaks in TC chromatograms were confirmed through integration following mass spectrometric detection (MS). It was necessary to compare the retention times of all detected species from multiple cells to demonstrate reproducibility along with assignment confirmation. **Table 1** summarizes the GC-MS/TCD qualitative results from a calendar (4.6 V, 55 °C) life test. The cells underwent formation (2 cycles), were charged to constant test voltage of 4.6 V, then placed in a 55 °C oven. The cell volumes and OCV's were monitored over a period of 3-4 weeks.

Table I: Gas Composition of LCO and NMC622 Cells as a Function of FEC Concentration

[FEC]	CH_4	C_2H_2	C_2H_4	C_2H_6	C_3H_6	C_4H_{10}	CH_3F	C_2H_5F	CO	CO_2	O_2	H_2	PF_3
LCO 10%	✓		✓	✓	✓	✓	✓	✓	✓	✓	✓		✓
LCO 20%	✓	✓		✓		✓	✓	✓	✓	✓	✓		
NMC622 10%	✓		✓	✓			✓	✓	✓	✓	✓	✓	
NMC622 20%	✓	✓		✓			✓	✓	✓	✓	✓	✓	

Two different concentrations of FEC (v/v %) were initially tested during the extended aging experiment. The LCO cathode cells with 10 % FEC exhibited the largest amount of gas produced at 4.6V, in addition to the only battery evolving the longer chained hydrocarbon gases.

In all batteries, CO_2 and CO are the largest components of the analyzed gas, originating from the breakdown of carbonate components (EC, FEC, and EMC). Also present are quantifiable amounts of methane, ethane, and O_2. Additional gases (PF_3, etc.) are present in trace, but measureable quantities. Although the NMC 622 cells produce quantifiable amounts of H_2, its presence in LCO cells cannot be ruled out due to detection limits (> 8.5 v/v %) when using helium as the carrier gas.

Relative integration ratios of detected gases provided insight into major/minor components in the mixtures. In the first batch of cells analyzed, the high-Ni containing NMC622 generated larger amounts of both fluorinated gases (CH_3F and CH_5F), however did not generate the longer chained hydrocarbons such as butane, propane, and propene. The likely mechanism of fluoromethane and fluoroethane formation is the breakdown of FEC at 4.6V. These were the only two hydrofluorocarbons (HFC's) detected in the gas mixtures. No fluorinated components originating from the fluoroether were detected in any high temperature OCV aging test further supporting its high temperature and high voltage stability in LiB's. PF_3 detected in the LCO cell at 4.6 V with 10% FEC can be attributed to decomposition of the $LiPF_6$ salt in the presence of moisture although the mechanism for formation is not currently understood. These cells were the only cell chemistry/electrolyte formulation where PF_3 was detected and no further investigation into this observation was pursued.

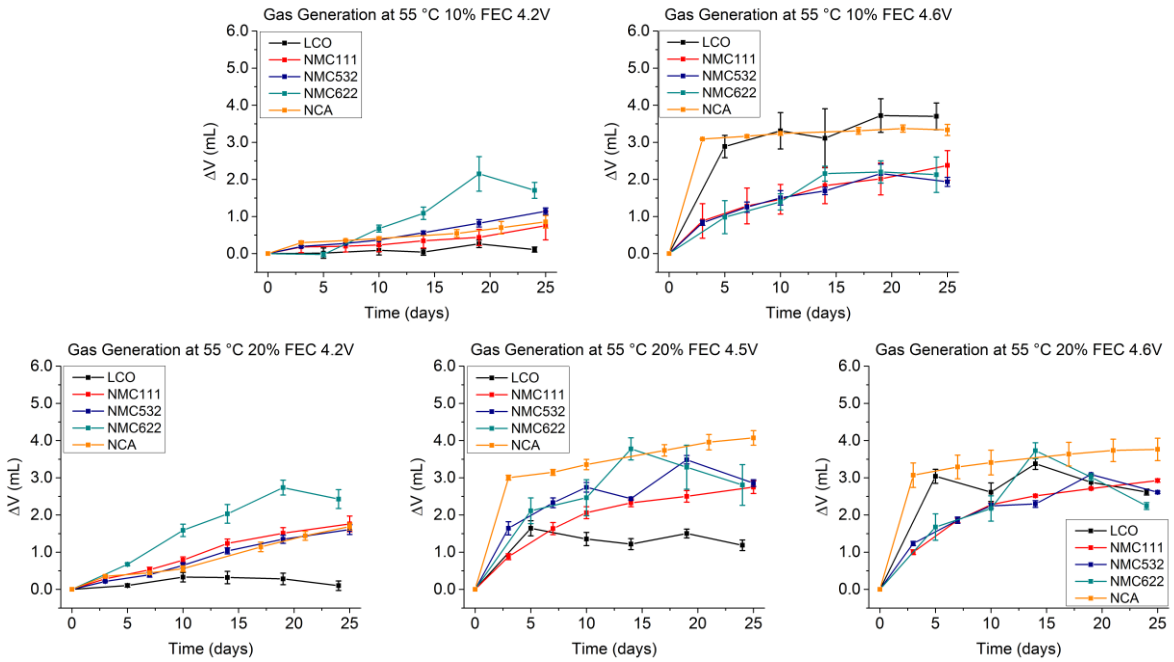

Figure 7: Gassing results as a function of cell chemistry and [FEC]. LCO and NCA produce the most gas at high voltage due to instability of the cathode. A higher [FEC] content in NMC containing cells results in more gas generation.

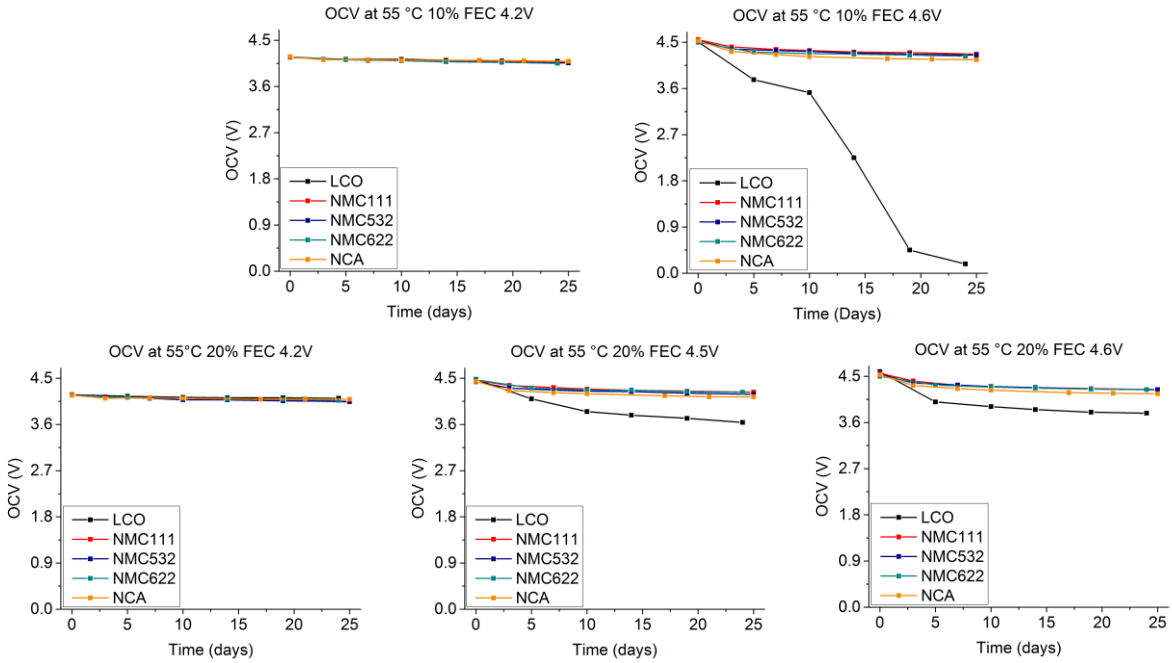

Figure 8: OCV results as a function of cell chemistry and [FEC] of the cells depicted in **Figure 7**. Measured declines in OCV are correlated to gas generation (**Figure 7**).

As a result of the initial testing with LCO and NMC622 cathodes, 55 °C was identified as the optimum temperature for gas generation as a function of cell chemistry. While 4.6V is the target for overall cell performance, benchmark performances at both 4.2 and 4.5V were also established. Depicted in **Figure 7** is ΔV (gas generation) versus time as a function of cell chemistry, voltage, and electrolyte formulation at elevated temperature. At 4.2V, cells produce

minimal gas, however, the amount does increase with a higher concentration of FEC. This observation suggests that even at 4.2V, FEC degrades at elevated temperatures in all cell chemistries tested throughout the project. OCV versus time of the cells depicted in **Figure 7** can be seen in **Figure 8**. One important takeaway from this comparison is that gas generation is correlated to a decreasing open circuit voltage and can be observed in all cathodes with both electrolyte formulations. In addition, the majority of gas produced during calendar life testing is within the first 240 hours. As a result, the first 240-hour time period became the focus of additional testing to quantitate identified gaseous components.

All cell chemistries show similar kinetic behavior within the first 240 hours of calendar life testing at high voltage. LCO and NCA do show increased gassing behavior at elevated temperatures, which is likely originating from the cathode materials themselves as opposed to increased degradation of the electrolyte. NMC111, 532, and 622 show similar behavior further supporting the notion that high-Ni NMC cathodes are ideal candidates for high voltage operation in LiB's.

Calibration curves are required in order to quantify the battery gas produced by the pouch cells. To get the highest degree of accuracy in the calibration curve, five or more calibration points were used, meaning at least five different percentages of each gas were required for GC-MS quantification. Instead of opting for purchasing standard gas mixtures from a supplier, an in-house custom gas manifold was fabricated in order to provide the most flexibility and cost effectiveness. In addition, calibration mixtures containing fluorocarbon gases (CH_3F and C_2H_5F) were not readily available, further supporting the need for the manifold to quantify these components. The gas mixing manifold was comprised of various stainless steel components with typical Swagelok® type fittings. **Figure 9** depicts the schematic of the gas manifold with all major components indicated.

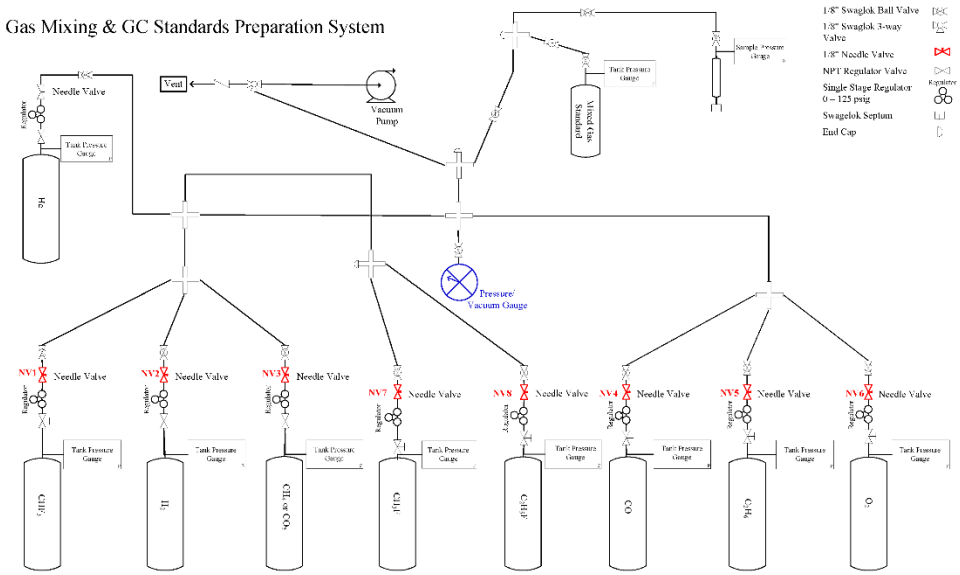

Figure 9: Schematic of the custom built gas mixing manifold to support quantification of gassing at high voltage

Standard gas mixtures that were created fell into three categories: Fluorocarbon (fluoromethane and fluoroethane), Oxygen-containing (oxygen, carbon dioxide, carbon monoxide), and Hydrocarbon (methane and ethane). Ethylene and hydrogen were not quantified

due to their low concentration and increased flammability, however, they are compatible in this type of system. Gases were mixed by controlling the flow from the cylinder (CGA-type regulator or flow controller) in combination with a ball valve and needle valve to reach the desired amount by monitoring the digital pressure gauge. The balance of each mixture was comprised of helium with all cylinders having identical pressures (± 1%). Calibration curves were generated for each individual component at a minimum of five (5) different concentrations with each concentration having three reproducible injections. The concentration ranges for each analyte were independent of one another, and were chosen from observations made throughout the project. All reported values fell within the concentration ranges of each component, with some analytes being below the limit of quantification (LOQ) of our instrumental setup.

Additional improvements to quantifying gaseous components in high voltage pouch cells were made in FY20. Major components were previously identified, however, separating low molecular weight species through GC/MS remained a challenge. In order to rectify this, a liquid nitrogen cryogenic valve (Agilent) and a corresponding 50L liquid nitrogen dewar were implemented to lower the initial temperature in the separation method to -10 °C. Without using cryogenic liquids, the separation/quantification of the lowest molecular species proved problematic (CO, CH_4, and O_2).

In addition to improving the analytical method for gas quantification using GC/MS, modifications to the pouch cell were performed in order to improve the gas extraction process. Previous reports have used airtight extraction chambers for pouch cells,[4] however, these methods significantly dilute the gas composition. A method was introduced to apply a 2-part coating to the outside of the pouch cell. This coating serves two purposes: 1) To form a seal around the needle when extracting gas using a gastight needle/syringe and 2) Enable multiple extractions/injections of gas extracted from a single pouch cell. Batteries were initially coated with a thin layer of adhesion promoter to prime the Mylar pouch, then hung freely to dry in a fume hood. The pouch cells were then submerged in solvent-based rubberized coating and hung to dry overnight. All injections were obtained using the same injection site from where the initial injection occurred to demonstrate the reproducibility of this method compared to the uncoated analog. No residual solvents were detected by the MSD from the coating process (i.e. Xylenes), supporting the required overnight cure time. **Figure 10** depicts an uncoated cell (left) and a typical coated cell (right) after calendar life testing.

Figure 10: Side-by-side visual comparison of pouch cells with (right) and without (left) the rubberized coating

No battery was known to generate N_2, the major component of air. As a result, the concentration of N_2 detected with the MSD can be correlated to the amount of atmospheric contamination in the method. Extractions were performed at the same location on the pouch cell. **Figure 11** depicts the volume change throughout the calendar life test (left) and the amount of air introduced during a manual extraction/injection from a pouch cell (right). In both methods of sample introduction, the first injection introduces approximately the same amount of air contamination. However, the two-layer coating reduces the amount of air introduced into the GC/MS if multiple injections from the pouch cell are targeted. Multiple gas injections allow for a more thorough understanding of the gassing kinetics and compositional information in cells as a function of time/voltage/electrolyte.

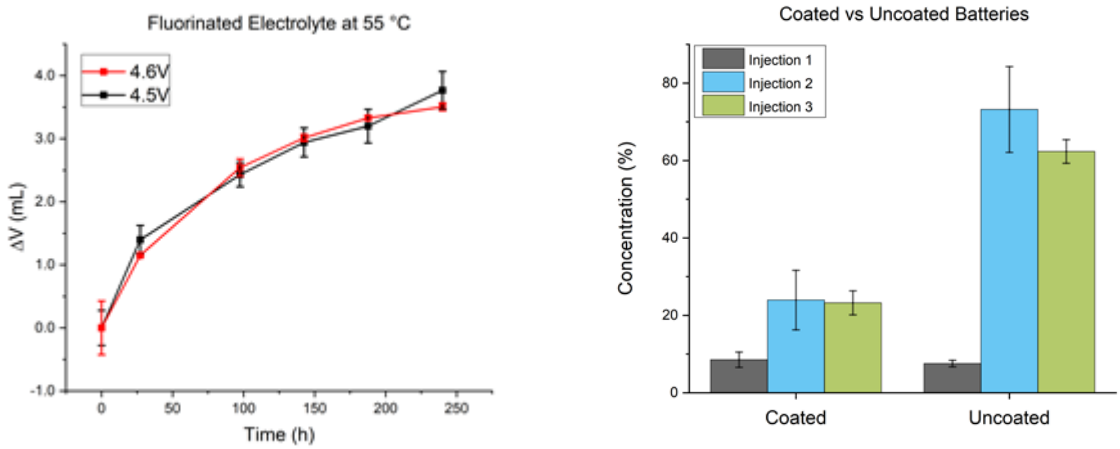

Figure 11: NMC622 pouch cells at 4.5 and 4.6V (left) with the fluorinated electrolyte (1.2M $LiPF_6$ 60:20:20 (EMC:HFE:FEC) + 1% PS). Atmospheric concentration when extracting/injecting gas manually using a gastight syringe (right). Data was obtained from coated and uncoated NMC622 cells with the fluorinated electrolyte at 4.6V.

In both methods of sample introduction, the first injection introduces approximately the same amount of air contamination. However, the two-layer coating reduces the amount of air introduced into the GC/MS if multiple injections from the pouch cell are targeted. Multiple gas injections allow for a more thorough understanding of the gassing kinetics and compositional information in cells as a function of time/voltage/electrolyte. It is important to note that H_2 and C_2H_4 were also detected in these cells, however, the concentrations were below the limit of detection (LOD) used herein. Three extractions were analyzed from each coated pouch cell, and performed immediately after one another with minimal dwell time between injections. As a result, the notion that by applying a flexible coating on the exterior of the pouch cell decreases atmospheric contamination in order to obtain multiple injections from a pouch cell. This technique of gas extraction/analysis can also be used widely by researchers who may not have access to more elaborate ways to approach gas analysis.

As observed in **Figure 11**, NMC622 with the same fluorinated electrolyte, evolved nominally the same amount of gas at both 4.5 and 4.6V. This suggests there is little difference in the total amount of gas at the two voltage thresholds, with more information needed on compositional differences. **Figure 12** depicts the quantitation results from NMC622/Graphite cells containing the 20% FEC electrolyte, at both 4.5 and 4.6V.

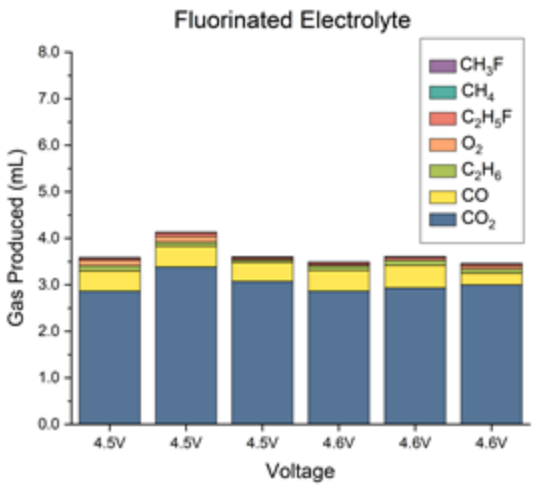

Figure 12: Gas quantitation data from two sets of three independent NMC622/Graphite cells are depicted containing the fluorinated electrolyte

At both voltages CO_2 is the major gaseous component at over 60% by volume in all cells quantified, with CO present as the second-most abundant species. All other components, mainly hydrocarbons and HFC's, are very minor components at less than 5% of the overall mixture in aged cells. While it has been shown that FEC enables high voltage cycling, it also begins to degrade at elevated temperatures and voltage. As seen in earlier results, any gaseous component originating from the fluoroether was not detected. This observation has held true across all formulations and cell chemistries, further supporting its high-voltage stability.

Along with analysis of gassing in high voltage cells, optimization of the electrolyte formulation was monitored through internal cycle life testing under ambient temperatures without external pressure applied to the pouch cells. **Figures 13** (4.5 V) and **14** (4.6 V) depict the electrochemical performance of 200 mAh pouch cells at 0.7C as a function of electrolyte formulation and cathode composition.

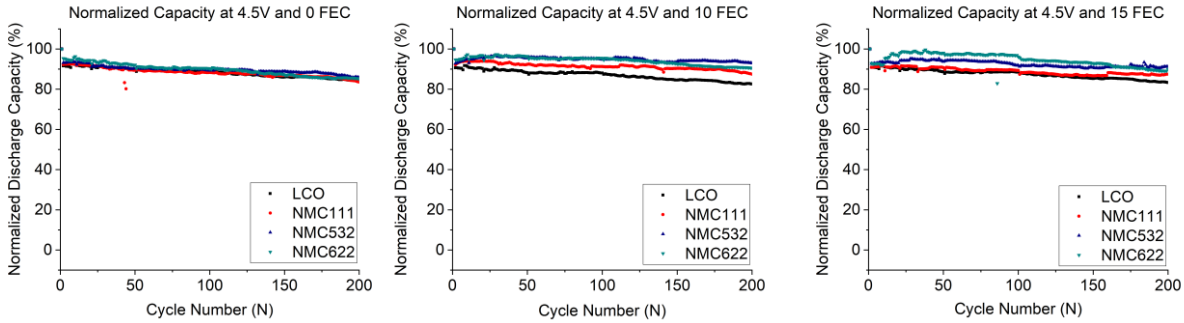

Figure 13: Cycle life testing as a function of cathode composition and electrolyte formulation at 4.5V. There is significant gassing that starts to occur at 4.5V, with FEC being a main contributor.

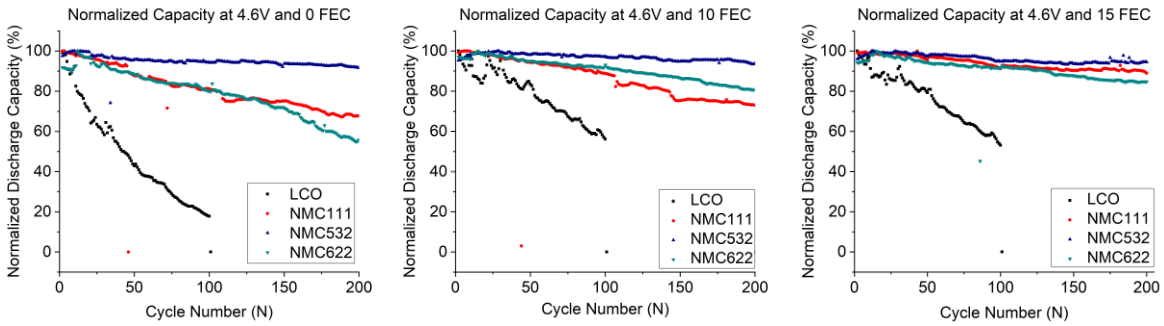

Figure 14: Cycle life testing as a function of cathode composition and electrolyte formulation. FEC is necessary to achieve performance at 4.6V with 15% (v/v) the optimized ratio in the electrolyte (right).

For cell operation at 4.6V, FEC is necessary to achieve the project's targeted electrochemical performance (> 80% capacity retention for at least 300 cycles). As depicted in **Figure 7** (bottom, middle), gassing starts to occur at 4.5V when FEC is present which is a possible explanation for the capacity decreases observed in cycle life testing with that upper cutoff voltage. Normalized discharge capacity analysis suggests that there are many suitable candidates for operation at both 4.5 and 4.6 V, however this data does not provide any insight into the energy density gains achieved by operating a battery at 4.6 V. As a result of this cycle life testing, NMC532/Graphite was identified as the most promising candidate for high voltage operation. While NMC622 would be the more preferable choice due to its increase Ni content (60 vs. 50%), NMC532 exhibited better capacity retention at 4.6 V in addition to a slightly small amount of gas produced at elevated temperature.

Current state-of-the-art lithium ion batteries used for electric vehicle applications have historically plateaued around 4.20 V with the liquid electrolyte being a major limiting factors. Increasing the operating voltage of each individual cell to 4.6 V by implementing a fluorinated electrolyte would significantly increase the EV's range and power availability. **Figure 15** depicts the 4.2 V versus 4.6 V specific discharge energy of 200 mAh as a function of electrolyte composition and cathode material at cycles: 10, 50, 100, 150, and 200.

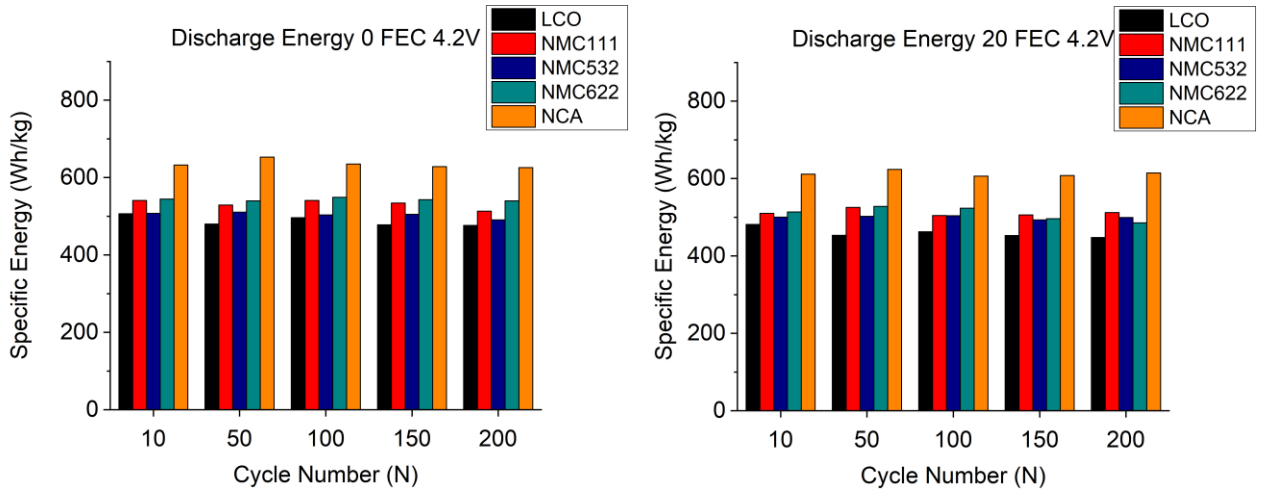

Figure 15: Specific energy analysis of cells containing either 0 or 20% (v/v) FEC in the electrolyte formulation, cycled between either 3.0 and 4.2 V (top) or 3.0 and 4.6 V (bottom)

At 4.2V, all cells show similar specific energies throughout the duration of testing. LCO and all NMC cell chemistries tested show similar retention through 200 cycles at approximately 500 Wh/kg. NCA does contain a slightly higher specific capacity at this lower voltage threshold, however gases significantly above 4.2V which prevented it from being further investigated.

4.6 V cells exhibited a significant increase in energy density, along with a noticeable effect the presence of FEC has on energy retention throughout the cell's lifetime. For example, NMC111 cells containing the 20% FEC electrolyte had a 38% higher specific energy after 200 cycles compared to cells without FEC. A similar observation is made with both NMC532 (8.5%) and NMC622 (67.8%), with the latter benefiting significantly from the presence of FEC in the electrolyte. Combining the information gained through capacity retention studies (**Figure 14**) with the specific energy analyses (**Figure 15**) has provided insight into the optimal cell chemistry and electrolyte formulation to achieve the overall goal to deliver a cell that is capable of cycling at 4.6 V for hundreds of cycles. Although NMC532 shows slightly lower specific energy than the higher-Ni containing NMC622 (**Figure 15**), its capacity retention and stability at high voltage make it better suited under these demanding conditions.

Gassing of the electrolyte is only one mechanism observed at high voltage that results in premature cell failure. Other interactions between the liquid electrolyte and active material in the cell occur concurrently, with not all being detrimental. One of these reactions results in an amorphous organic coating on the surface of the cathode. These are referred to the cathode-electrolyte interface, or CEI layer.[17] Analysis of electrochemical data obtained throughout the project supports the hypothesis that highly fluorinated electrolytes perform better above 4.5V when compared to their hydrocarbon analogues. A possibility is that fluorinated components, which are more resistive to oxidation, do not completely decompose to form gas. Instead, a protective film is formed on the cathode surface further protecting the electrolyte from oxidation.

The project aims to develop a method and identify various analytical tools which can achieve two goals: 1) Determine the CEI layer's chemical composition and 2) Measure the film thickness on the surface. To determine the CEI layer's composition, AES was implemented due to its high sensitivity and spatial resolution. The drawback to using AES is that the information it provides is limited to elemental sensitivity, with little extractible chemical information. **Figure 16** depicts elemental survey scans of a dried, uncycled NMC622 cathode (left) and a post-mortem NMC622 cathode extracted from a cell containing a highly fluorinated electrolyte; 1.2M $LiPF_6$, 60:20:20 (EMC:HFE:FEC)+ 1% PS. Survey spectra were obtained both before and after depth profiling using an Ar^+ ion gun.

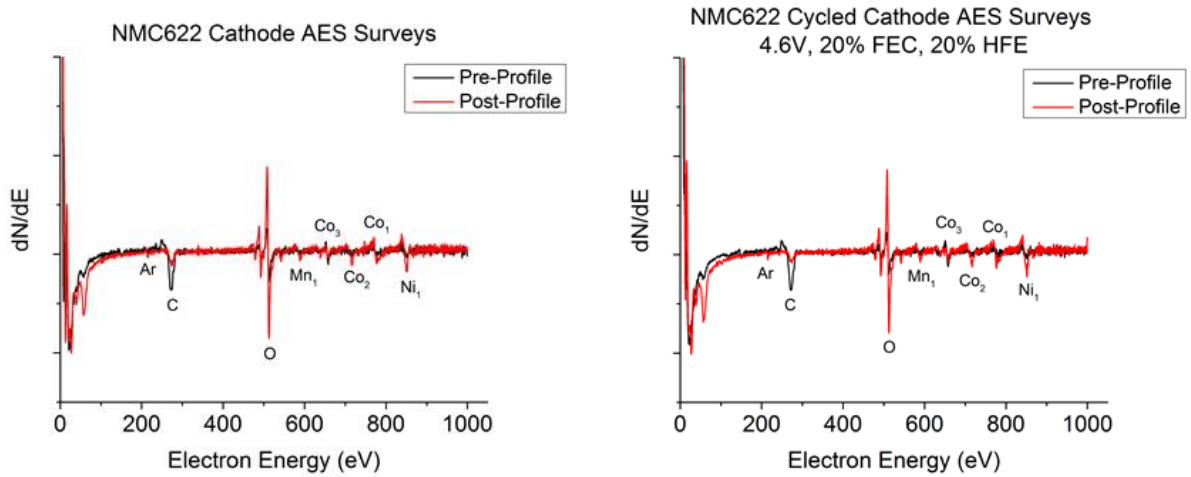

Figure 16: AES survey scan of a pristine (left) and cycled (right) NMC622 cathode both before (**black**) and after (**red**) a brief depth profile

Evident in the pre-depth profile survey scans (**Figure 16**) are similarities between the pristine and cycled NMC622 cathodes. Oxygen exhibits the strongest Auger signal with Carbon also present with high intensity. The oxygen signal arises from the bulk $LiNi_{0.60}Mn_{0.20}Co_{0.20}O_2$ structure, with minimal contributions from any surface species. The carbon originates from multiple sources with the largest two being adventitious carbon and PVdF binder.[17-20] Also measureable are the signals from the transition metals in the cathode (Ni, Mn, Co) and to a lesser extent Fluorine. As the surface species are sputtered away during the depth profile, the Auger signal from the transition metals and oxygen becomes more intense (red traces versus black). Although the majority of carbon-containing substances are superficial, there will always remain a strong signal from the PVdF bind and conductive carbon black throughout the cathode. Although the elemental composition of a pristine and electrochemically tested cathode are identical, variances between the two are overlooked with AES. In order to further probe the chemical makeup of the amorphous film on the cathode surface, Time-of-Flight Secondary Ion Mass Spectrometry imaging was performed in collaboration with Physical Electronics USA (PHI). TOF-SIMS offers the spatial and surface sensitivity seen in AES, but with the added benefit of providing high-resolution mass spectra.

To probe differences in surface chemical composition as a function of electrolyte, cathodes from two identically tested NMC622/Graphite cells were extracted and analyzed with TOF-SIMS. Both cells were cycled between 3.0 and 4.6V, one with the hydrocarbon electrolyte (1.2M $LiPF_6$, 80:20 (EMC:EC) + 1% PS), and the other with the fully fluorinated analog (1.2M $LiPF_6$, 60:20:20 (EMC:HFE:FEC) + 1% PS). Residual electrolyte was allowed to evaporate prior to analysis, and placed in the UHV load lock exposed to a turbo pump to allow any residual species to off-gas. **Figure 17** depicts the spatial distribution and relative intensity of relevant (+) secondary ions seen with the hydrocarbon electrolyte.

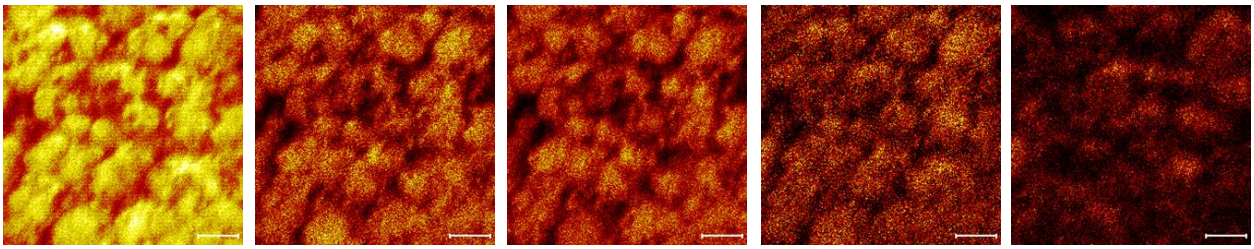

Figure 17: Selected (+) secondary ions detected with spatial intensity with the hydrocarbon analog. From left to right the color plots represent: TIC^+, $^{58}Ni^+/^{60}Ni^+$, $^{55}Mn^+$, $^{59}Co^+$, and $C_xH_yLi^+$ (m/z = 58, 59, 85)

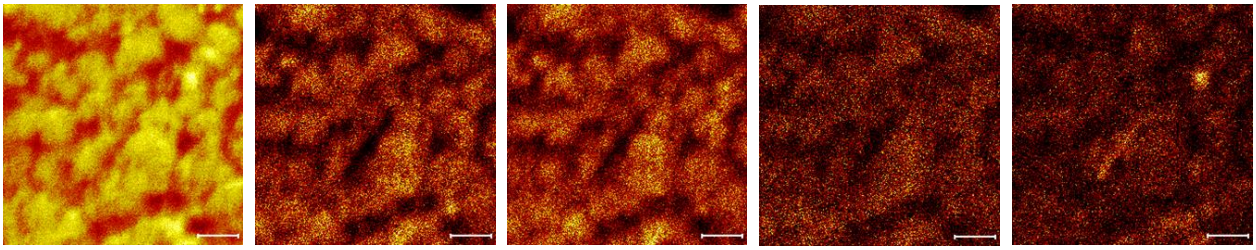

Figure 18: Selected (+) secondary ions detected with spatial intensity with the fluorinated analog. From left to right the color plots represent: TIC^+, $^{58}Ni^+/^{60}Ni^+$, $^{55}Mn^+$, $^{59}Co^+$, and $C_xH_yLi^+$ (m/z = 58, 59, 85)

Figures 17 and **18** represent identical (+) ions detected on the surface of both cathodes. Both samples were thoroughly degassed prior to loading into the UHV chamber, and it is unlikely liquid electrolyte is contributing to these signals. Both samples show similar species on the surface, with the majority originating from the cathode particles themselves. However, there are lithiated organic fragments present (right most plots) on the surface with noticeable intensity (m/z = 58, 59, 85). These hydrocarbon species suggest that a hydrocarbon also contributes to the film formation on the cathode, with EMC, EC, being contributors.

While lithiated species are anticipated in the (+) mode, any highly fluorinated or organic species is expected to be detected as (-) secondary ions. **Figures 19** and **20** depict these negative secondary ions detected in both NMC622 cathodes as a function of electrolyte.

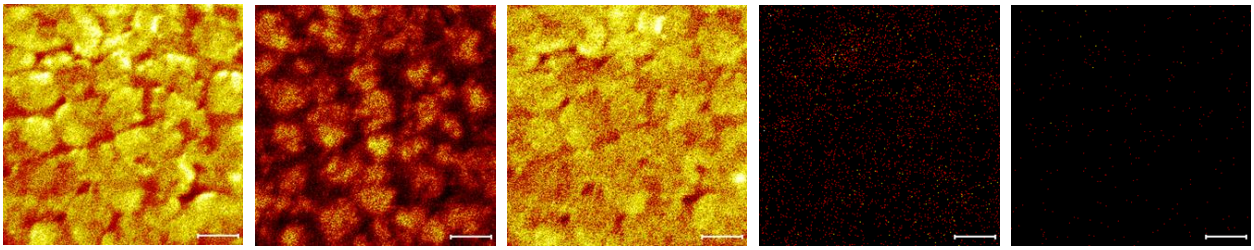

Figure 19: Selected (-) secondary ions detected with spatial intensity with the hydrocarbon electorlyte. From left to right the color plots represent: TIC^-, $^{16}O^-$, $^{19}F^-$, $C_xH_yF_zP_w^-$ (m/z = 103, 105, 108), and $C_xH_yO_zF_w^-$ (m/z = 79, 80, 81)

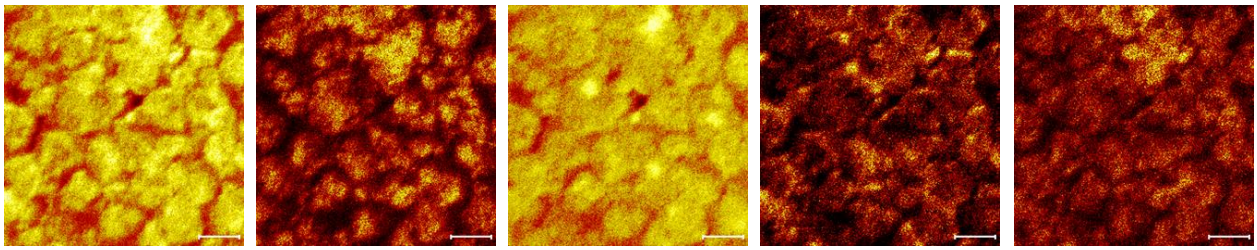

Figure 20: Selected (-) secondary ions detected with spatial intensity with the fluorinated analog. From left to right the color plots represent: TIC^-, $^{16}O^-$, $^{19}F^-$, $C_xH_yF_zP_w^-$ (m/z = 103, 105, 108), and $C_xH_yO_zF_w^-$ (m/z = 79, 80, 81)

The negative ion modes of both cathodes show similar intensity in TIC^-, however, the chemical composition of the surfaces show significant differences. A strong signal originates from the cathode particles which is detected as $^{16}O^-$. $^{19}F^-$ is also present in both cathodes, with the majority of signal arising from the surface of the particles. $LiPF_6$ and its degradation products are the most likely origin, with a smaller concentration from the PVdF binder. The low intensity visible in the valleys between particles is also likely binder in origin, with permeated salt as a minor contributor. Notable differences occur in the detection of fluorinated organic species. These are absent in the hydrocarbon electrolyte samples (**Figure 19**, right), but show a strong presence with the fluorinated electrolyte (**Figure 20**, right). While there are detectable organic species in both cases and are elementally identical in the AES spectra, the chemical composition varies as a function of electrolyte. Organic fragments in both NMC622 cathodes did not show any repeatable mass fragments on the surface, suggesting that there is no controlled polymerization of the organic electrolyte at the interface of the cathode.

Determining the film thickness was carried out using AES, utilizing both survey spectra and Ar^+ ion depth profiles. Through TOF-SIMS and AES, superficial species on the cathode are carbon-containing and largely an organic species. Traditional depth profiles used in AES to determine film thicknesses are calibrated to the native oxide layer in SiO_2 (1000 Å). A more accurate method to determine the carbon-containing CEI layer is necessary, using a carbon film standard. To perform this, amorphous carbon films were grown on silicon wafer surfaces externally (UHV Sputtering, Inc.) to serve as the sputter rate calibrant. Three separate carbon film thicknesses were created (50, 100, and 500 nm), which were deposited on 100 nm thick aluminum layers. The purpose of the aluminum layer was to serve as an IR reflector to support auxiliary experiments, and also as an elemental marker for cross-sectional imaging.

Prior to calibrating the Ar^+ ion gun to perform depth profiles, it was necessary to confirm the exact film thicknesses of the three different carbon layers. Focused Ion Beam (FIB) and SEM imaging were performed in collaboration with a 3rd party test laboratory to measure these

thicknesses with high resolution imaging. **Figures 21-23** depict the cross sections of each different thickness standard, with labeled film thickness determinations.

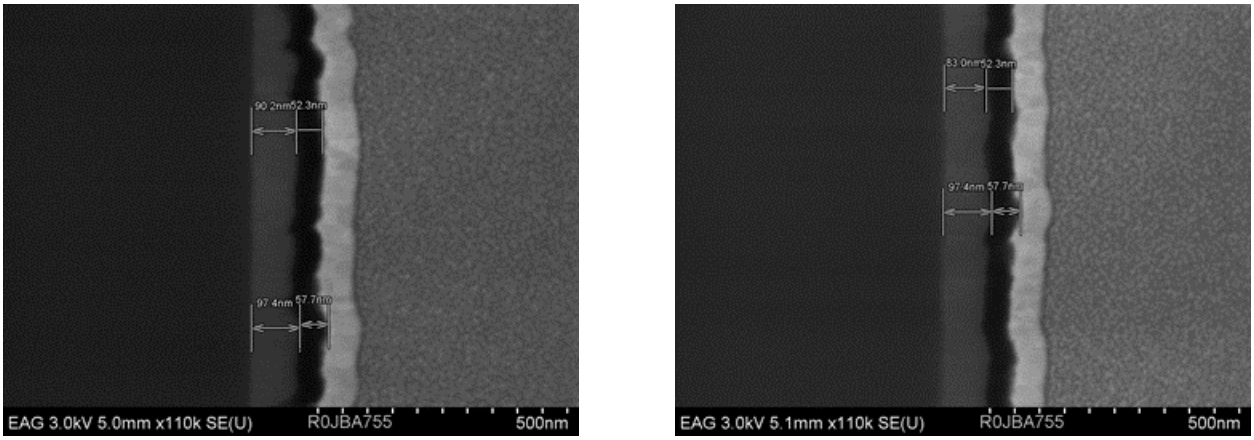

Figure 21: Representative FIB-cut cross sections with high-resolution SEM images. The carbon layer is seen as the thin black film between the aluminum (left) and sputtered Pt (right). Average thickness of the film standard is 54.2 nm

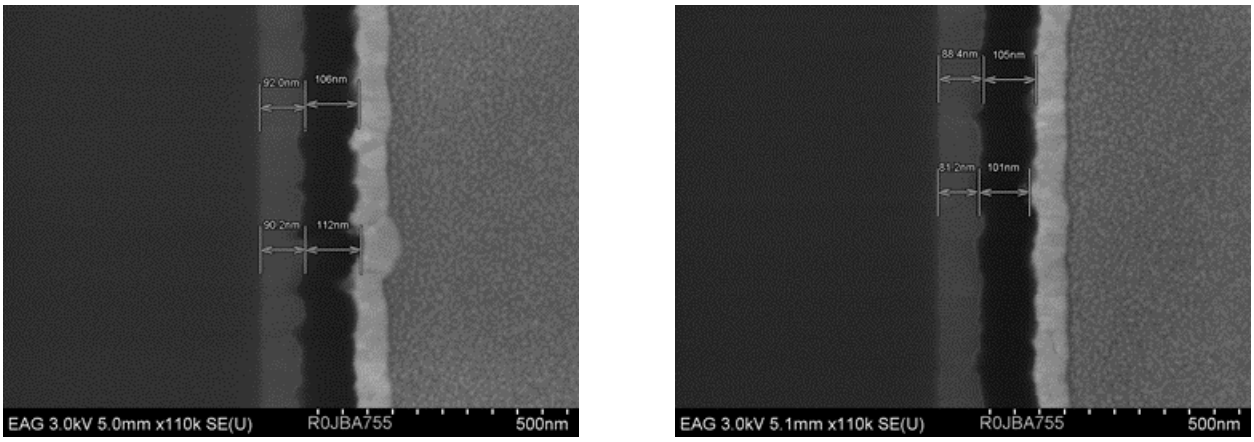

Figure 22: Representative FIB-cut cross sections with high-resolution SEM images. The carbon layer is seen as the thin black film between the aluminum (left) and sputtered Pt (right). Average thickness of the film standard is 108 nm

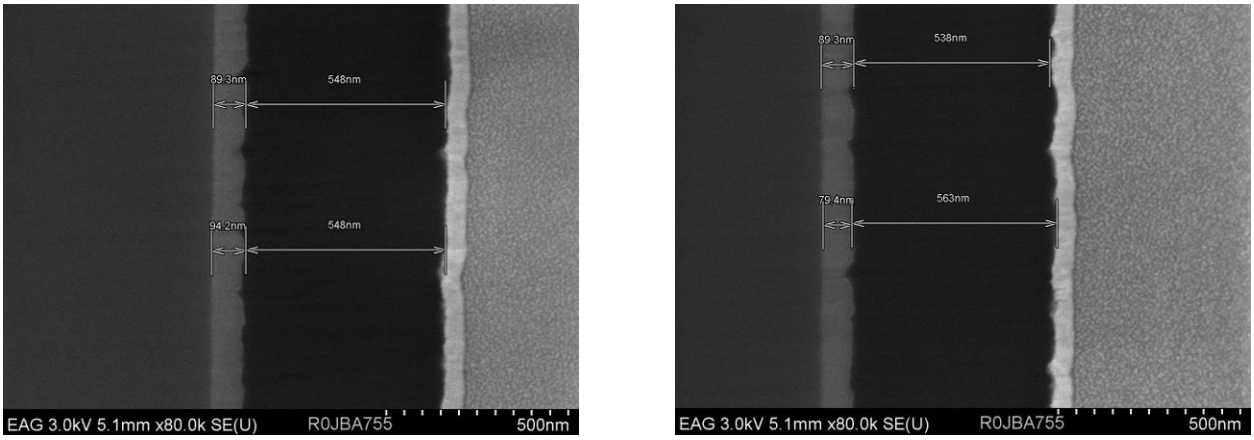

Figure 23: Representative FIB-cut cross sections with high-resolution SEM images. The carbon layer is seen as the thin black film between the aluminum (left) and sputtered Pt (right). Average thickness of the film standard is 551 nm

The targeted sputter rate of the Ar^+ ion gun for determining the film thicknesses was determined to be 1 nm of equivalent carbon per cycle. **Figure 24** depicts the elemental intensity during calibration trials of the different carbon standards. The initial layer during the carbon standard depth profiles is carbon, followed by aluminum, and lastly the silicon wafer. The layer is completely removed when the signal reached a minimum in the AES intensity plots.

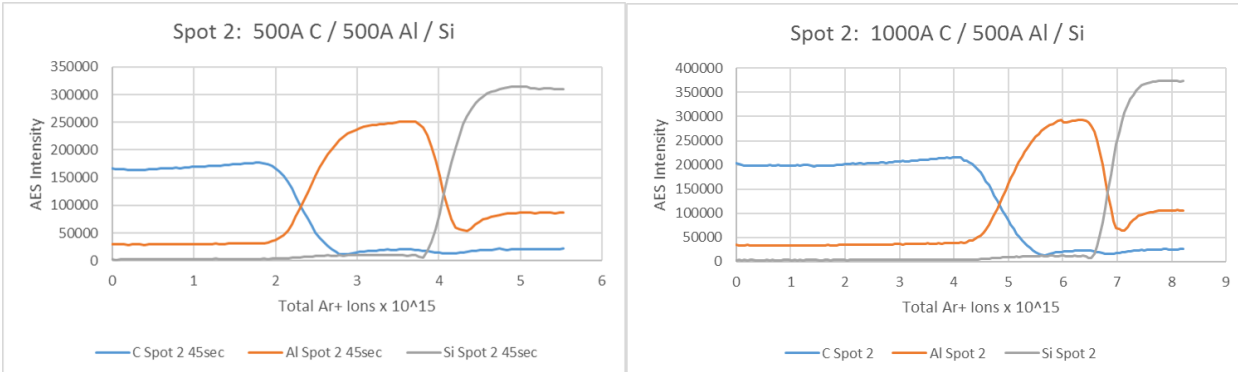

Figure 24: Representative depth profiles of the 54 nm carbon film standard (left) and the 108 nm standard (right). As the carbon layer is sputtered away, the aluminum components is detected. Ultimately both layers are removed, exposing the silicon wafer substrate.

The data is plotted as total Ar^+ dose rather than by sputter cycle to account for variances in ion intensity amongst replicates. This is calculated by measuring the current on the analytical stage. The pressure of the ion gun was maintained at a constant 17.5 mPa, at which the current was measured both before and after the depth profile with the AES electron gun off. **Figure 25** depicts the sputtered area following a depth profile using the SEM on the AES, with the 54 nm (left) and 108 nm standard (right).

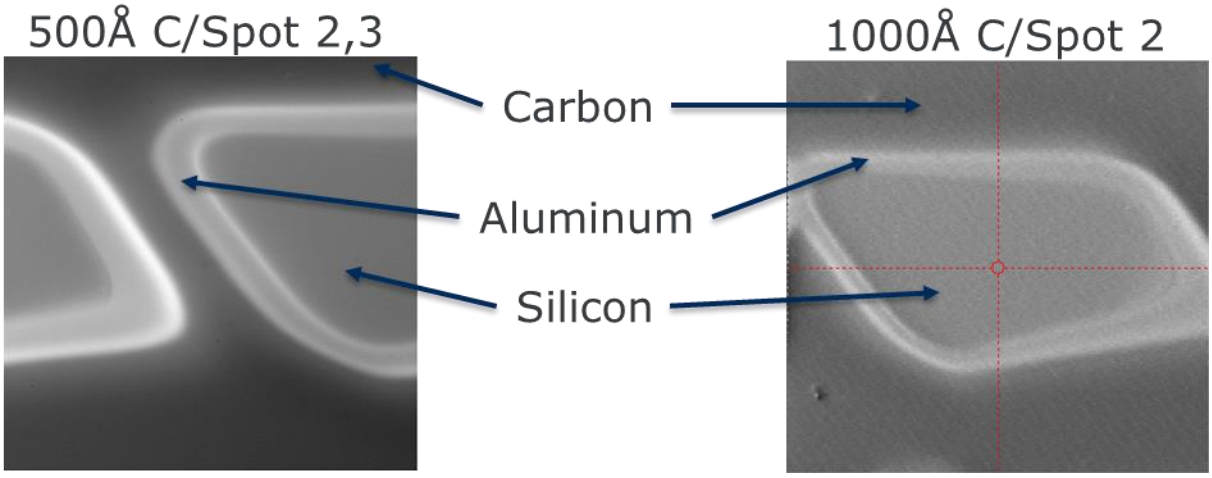

Figure 25: The sputtered are of the sample is indicated above for both standards. The red crosshair visible in the 108 nm standard image indicates the electron beam impact position. This is where AES measurements are obtained, which is centered inside the analytical area of interest.

Multiple spots on both the 54 nm (500 Å) and 108 nm (1000 Å) carbon standards were depth profiled in order to build up a statistically meaningful dataset. Along with this, a 1 cm x 1 cm raster area for the ion gun was used for all depth profiles to take advantage of area averaging for a more accurate determination. **Figure 26** depicts average AES signals from depth profile

experiments performed on both a cycled (4.6V, 1.2M $LiPF_6$ 60:20:20 (EMC:FEC:HFE) + 1% PS) and pristine NMC622 cathode. Carbon, Oxygen, and Nickel were the elements used to track the progress of all depth profiles due to their relevance to the different layers. These depth profiles relate the AES signal for each element in relation to total Ar^+ dose. The difference in the average ion current to reach the Carbon-Oxygen intercept is representative of the total CEI layer's thickness in the cycled battery. Carbon serves as the spectroscopic handle to monitor the progression of the depth profile through the CEI layer, whereas Oxygen and Nickel indicate the surface of the cathode particles.

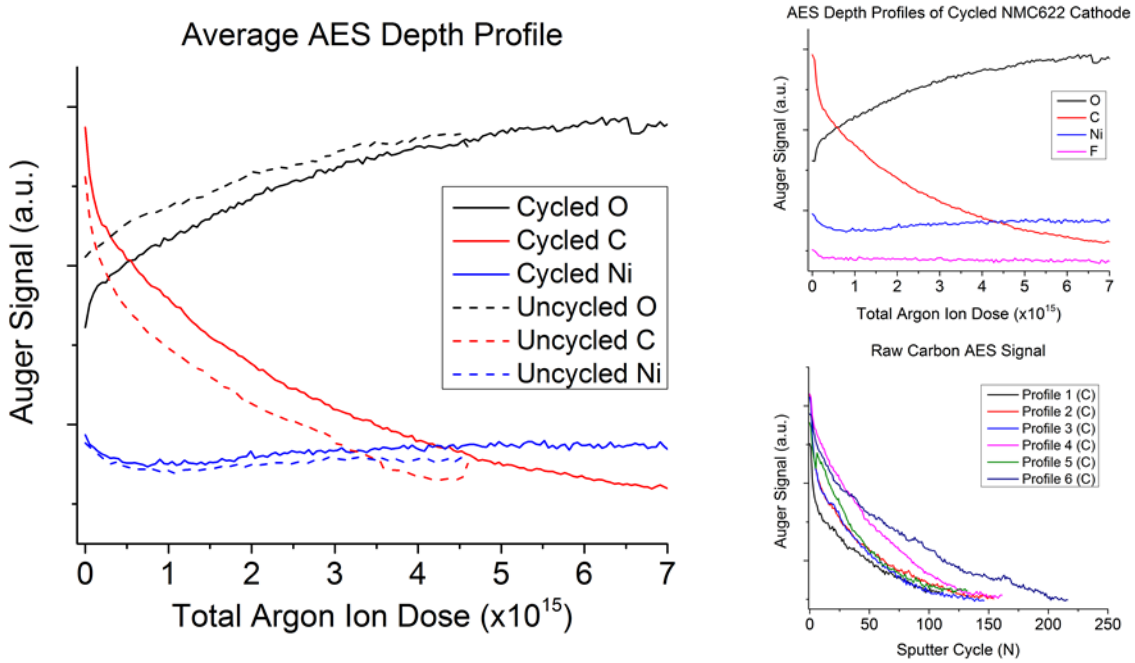

Figure 26: Average depth profile data of different spots on an NMC622 cathode (left). Solid lines represent that from a cycled cathode (4.6 V, fluorinated electrolyte), dashed lines from an uncycled cathode. Average AES signal of cycled NMC622 cathode (top right). Raw carbon AES signal from each depth profile contributing to the average (bottom right).

Once the data sets for both a pristine and cycled NMC622 cathode were obtained, the average signals of C, O, and Ni were compared side-by-side to back out the film thickness. **Figure 27** depicts both the average signal from the pristine NMC622 dataset (left) and the 4.6V cycled NMC622 with fluorinated electrolyte dataset (right).

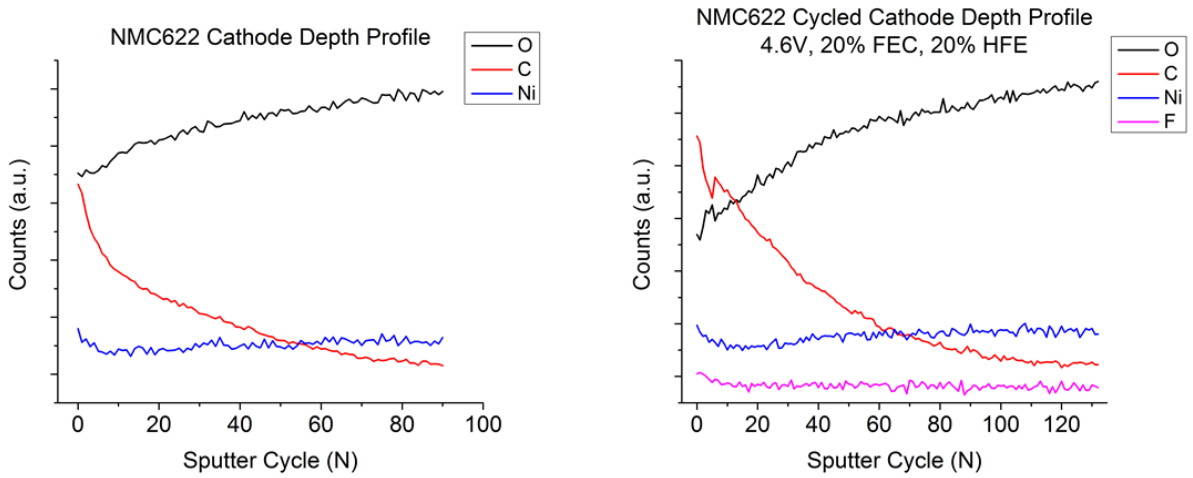

Figure 27: Average AES signal for a pristine NMC622 (left) and cycled (right) cathode. O, C, and Ni serve as the analytes of interest. The signal for Fluorine remains constant throughout the depth profile, with the major contributor to the signal being PVdF binder.

The position of the C-O intercept is correlated to the breakthrough point of the CEI layer where the majority of the AES signal arises from the cathode particles themselves as opposed to the superficial film. On average, the cycled cathode with fluorinated electrolyte requires 24-29 additional sputter cycles to diminish the carbon signal (**Figure 27**). This translates to a CEI layer thickness of 24-29 nm, which is largely carbonaceous in nature. These reported results are consistent with what has been reported previously, and provides valuable insight into the role fluorinated electrolytes play in high voltage lithium ion batteries.[17,20]

Interim cells were submitted to the Department of Energy to compare the electrochemical performance of optimized cell chemistry/electrolyte to that of the benchmark formulation. These cells should show a significant improvement over the initial cells submitted at the commencement of the project. 200 mAh NMC532/Graphite pouch cells were submitted for analysis. The benchmark hydrocarbon (HC) electrolyte was compared to the optimized fluorinated (FC) formulation (1.2M $LiPF_6$ 60:20:15:5 (EMC:HFE:FEC:EC)+ 1% PS) mid-way through the project. Cells were dosed with electrolyte volumetrically, which led to the fluorinated cells having a slightly higher mass due to formulation's increased density. Cells were formed at Daikin and then shipped to Idaho National Laboratory for testing. **Figure 28** depicts the static capacity of the data set, comparing HC and FC at both 4.5 and 4.6V.

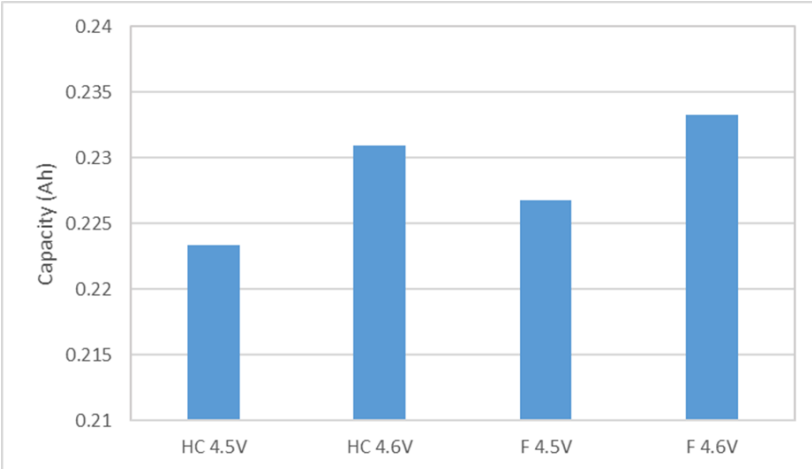

Average Capacity	
HC at 4.5V	0.223 ± 0.004 Ah
HC at 4.6V	0.231 ± 0.003 Ah
F at 4.5V	0.228 ± 0.002 Ah
F at 4.6V	0.233 ± 0.002 Ah

Figure 28: FC cells have higher initial capacity than HC cells at both voltages. Cells were balanced to 4.4V, causing the increased observed capacity (> 200 mAh) at high voltage

A higher initial capacity is observed for all FC cells when compared to the baseline HC formulation. This is attributed to the increased oxidative stability of the fluorinated analog at high voltage resulting in the increased energy density of the cells. Three cells per condition were cycled at 0.7C (140 mA) with 3.0V as the lower threshold, and the upper cutoff voltage designated as either 4.5 or 4.6V. **Figure 29** depicts DC resistance growth at each test point amongst all four groups of cells. 80% capacity retention serves as the threshold for performance, with ≥ 80% at 4.6V for at least 300 cycles the overall project target.

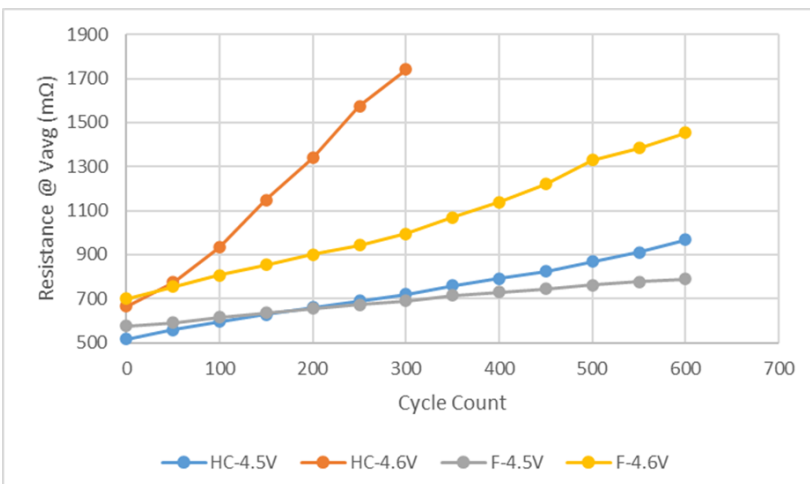

Avg. Resistance (RPT12)	
HC at 4.5V	968.3 ± 40.9 mΩ
HC at 4.6V	N/A
F at 4.5V	789.6 ± 69.3 mΩ
F at 4.6V	1453 ± 139 mΩ

Figure 29: Overall cell resistance of each group of tested cells. Aside from an increased initial resistance, the optimized fluorinated electrolyte outperforms the baseline HC electrolyte at both upper voltage limits.

FC cells show a slightly elevated DC resistance at both test conditions likely originating from the reduced conductivity when using fluorinated materials. However, the HC cells show accelerated resistance rise due to the instability of the hydrocarbon components at the upper voltages. In all four groups of cells, continuous resistance growth is observed and correlated to continuous capacity loss.

Swelling of the anode/cathode wind of 1 Ah NMC111 pouch cells was reported in previous findings (DOE EE0006437) and is a known degradation mechanism especially at high-voltage (> 4.5V).[1] Understanding how thickness changes as a function of time/voltage occur as a function of cell chemistry/electrolyte were targeted. It is hypothesized that this swelling is attributed to changes in the graphite anode. The initial approach to determine thickness changes (non-gassing) was performed using Keyence GT2 series contact sensors. The sensors were secured in place using custom fabricated/machined aluminum housings with insulating tape applied to the base to prevent accidental short-circuiting. Signal collected from the sensors were measured through the analog output leads (Voltage/Current) and recorded using a channel on an Arbin battery tester. These contact sensors have a linear response in the 0 – 5 mm range, with a ± .1 μm accuracy. Thickness standards (0 – 1 mm) were used to generate the calibration curve depicted in **Figure 30** (left). It was necessary to generate calibration curves for each sensor to account for system variability (Δ Thickness vs. Voltage). In addition, the layout of the contact sensor device for these 200 mAh cells can be seen in **Figure 30**.

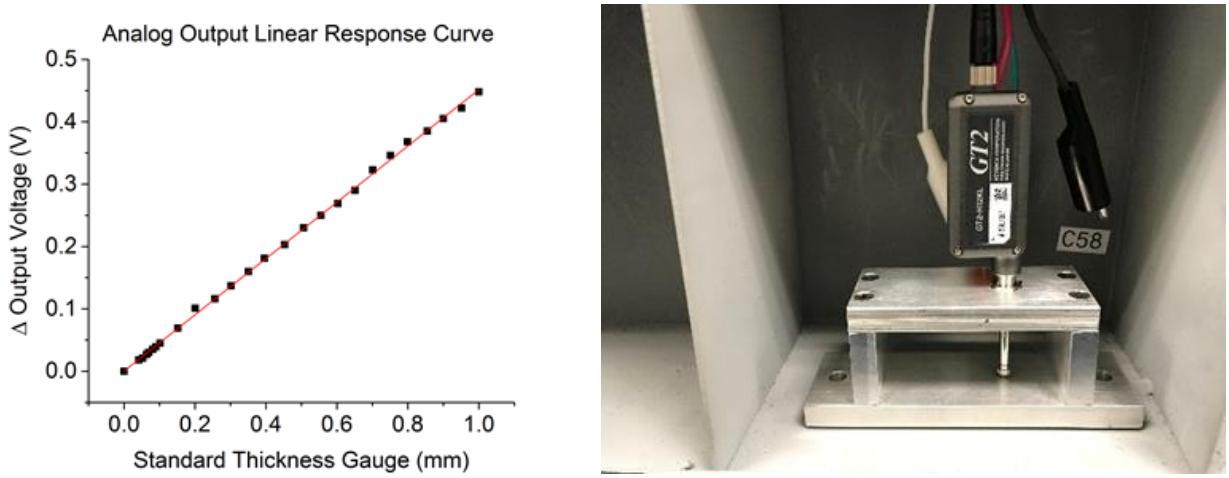

Figure 30: Linear response of the analog output from a GT2 sensor in the 0-1 mm range (left). Custom built setup to measure *in-operando* changes along the z-axis (thickness) of a 200 mAh pouch cell.

The initial experiments investigating NMC532 cells as a function of time/voltage/electrolyte were targeted due to it being the best performing cell chemistry to date. Three electrolyte formulations were included in the first batch of cells and were cycled at 4.2, 4.5, and 4.6V. Cells contained the identical $LiPF_6$ concentration (1.2 M) and 1,3-propane sultone (PS) as an anti-gassing additive (1% w/w). The HFE electrolyte contains 60:20:20 (EMC:EC:HFE), HFE/FEC electrolyte contains 60:20:20, and the baseline hydrocarbon formulation is 80:20 (EMC:EC). There are minimal changes to thicknesses in NMC532 cells at 4.2V when comparing hydrocarbon to HFE electrolyte. **Figure 31** depicts the thickness changes of NMC532 cathodes as a function of electrolyte over 200 charge/discharge cycles (symmetric CC charge/discharge at 0.7C, CCCV every 10) between 3.0 and 4.6 V.

As the cells lose capacity due to cathode/electrolyte degradation at high voltage, there is a measureable thickness increase as a function of cycle number. There is also a correlation between the accelerated thickness increase and capacity loss around cycle 150 in the NMC532 cell with the

hydrocarbon electrolyte (**Figure 31**, left and right). A major drawback to this method of measurement is that physical contact with the pouch cell applies force at the sensor/pouch interface resulting in the negative feature in both graphs.

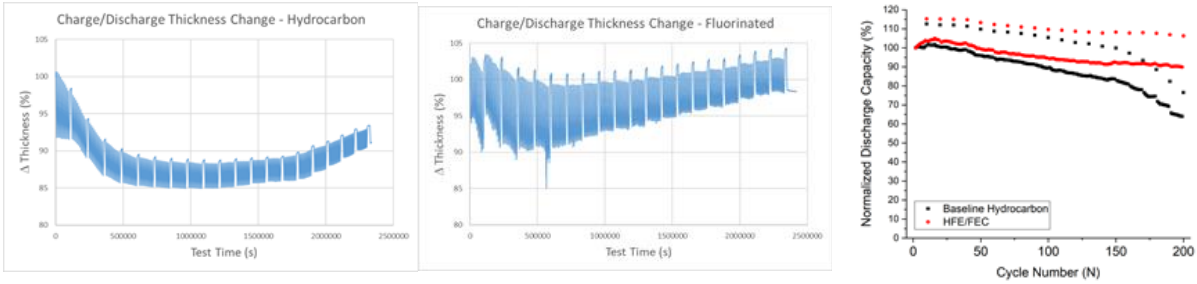

Figure 31: Thickness changes of NMC532 cells as a function of electrolyte, with the baseline hydrocarbon (left) and HFE/FEC electrolyte (middle). Electrochemical performance of NMC532 cells normalized to 1st CC cycle (right).

The Δ thickness on a per cycle basis has a fast and repeatable response, however, the compression of the cell at the contact point inhibits an accurate representation of the macro trend of pouch cell swelling. To attain a more accurate measurement in cell thickness changes (non-gassing), an alternative method as a function of time/voltage was designed. This method utilizes a fixed laser, which reflects off the surface of a fixed object at a glancing angle (29°), and can be thought of as a pseudo interferometer. The position of the reflected light is tracked with time-resolved photography and calibrated to known changes in position along the z-axis. This method of thickness measurement offers a ± 50 μm resolution and a repeatable response. Data can be depicted on a micro scale being the cycle-by-cycle comparison, or as changes of the cell throughout duration of the experiment. **Figure 32** depicts a schematic of the instrumental components, along with representative photos of a typical experiment during setup prior to starting the cycle life data acquisition.

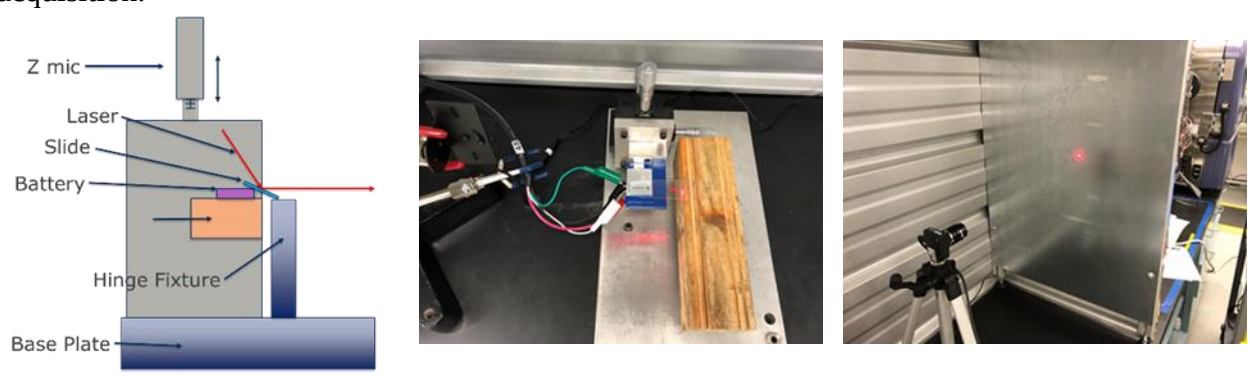

Figure 22: Schematic of pseudo interferometer apparatus to correlate pouch cell swelling with laser position (left). Representative photo of a pouch cell with reflected laser point off the glass slide (middle). Reflected laser point is tracked with a time-lapsed photo program (right). An opaque surface was using to track the position during the experiment in order to minimize refraction of the laser.

Prior to start-up, the battery undergoes formation unattached to the thickness instrument and is then discharged to 3.0V. Manual thickness measurements are obtained using a handheld micrometer to correlate results obtained using the reported instrument. Seven separate regions of the pouch cell are measured to obtain an understanding of the cell as a whole. Thickness measurements post-testing are obtained in the same areas, and at the same SOC to minimize

discrepancies due to anodic Li ion intercalation effects. Once these are obtained, the pouch cell is affixed to the apparatus to generate a laser position vs. z-height calibration curve. **Figure 33** depicts the calibration curve generated for the NMC532 cell reported herein.

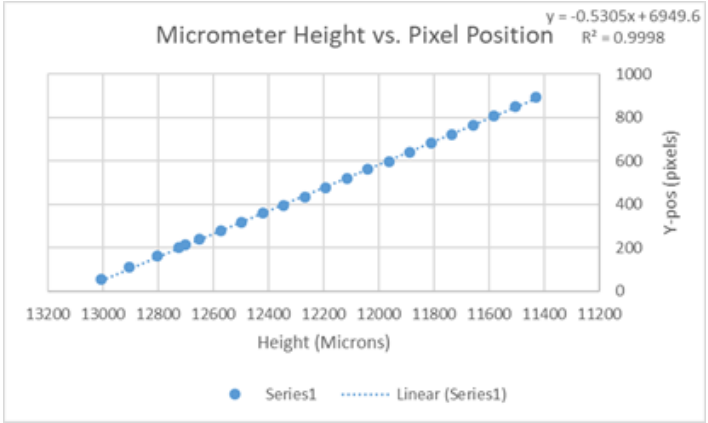

Figure 33: Pixel position vs. changes in height of the pouch cell are compared to the calibration curve depicted above. From this, Δ thickness from the starting point (%) is calculated.

The NMC532 cell reported contained the project baseline hydrocarbon electrolyte, and cycled at C/2 between 3.0 and 4.6V, with a CC-CV charge cycle performed every 10 cycles (C/20). Both electrochemical and pixel position data was recorded every 10 seconds. When at a 100% SOC, the pouch cell is at its greatest thickness due to the amount of Li intercalated within the graphite anode. When discharged, the pouch reverts to its minima, provided the thickness change avoids hysteresis. The macro-trend in the Δ thickness vs. cycle number/SOC can be attributed to irreversible changes to the pouch cell's thickness, and not gas generation. **Figure 34** depicts the electrochemical data of the cell throughout the duration of the experiment, along with the thickness change (non-gas) vs. cycle number.

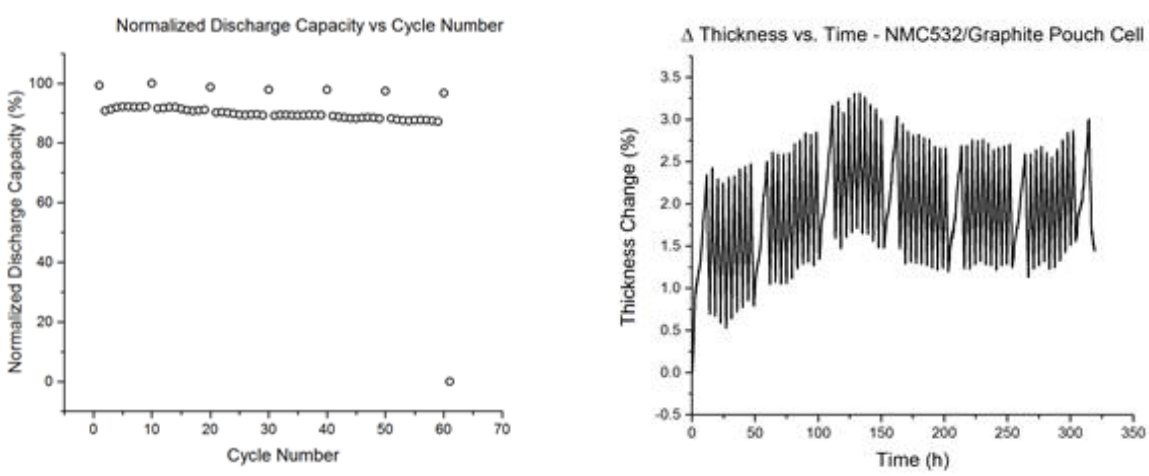

Figure 34: After 60 cycles, the NMC532 cell exhibits minimal capacity loss (left). Δ thickness versus time (right). The CC-CV cycles are represented by the longer charge durations.

On a cycle-by-cycle basis, the NMC532 cell displays a reversible thickness change of approximately 1.5%, which is consistent with other methods.[21-23] This is nominally repeated throughout the 60 cycles reported with minimal variation between cycles. When looking at the macroscopic trend as seen in **Figure 34** (right), there appears to be two periods of irreversible

thickness growth in the cell. The first of which can be seen between cycles 0 and 25, with the second arising around cycle 50 and continuing on until the end of the test. A potential explanation for the initial thickness change could be the continual build-up of the SEI layer on the graphite anode early on in the test. It is known that the majority of the SEI evolves throughout formation, however, can continuously grow depending operating conditions (C-rate, voltage, etc.) and chemistry (cathode, anode, electrolyte) of the cell. Since this cell was cycled up to 4.6V, a continuous build-up due to high voltage operation is a likely contributor to this. The second thickness growth region identified can be correlated to an acceleration of capacity loss near the conclusion of the test. This irreversible trend in the Δ thickness is minimal, but observable. Although these changes are above the instrument's LOD, these minor trend observations are within the method's experimental error.

Table 2 depicts the obtained values from external micrometer measurements, both before and after the test and **Figure 35** depicts the specific test points of the pouch cell's jellyroll where the physical micrometer measurements were obtained.

Table 2: NMC532 Pouch Cell Thickness by Region

Spot Location	Thickness Before (mm)	Avg Thickness Before (mm)	Thickness After (mm)	Avg Thickness After (mm)	% Increase
1	3.618	3.687	3.808	3.823	3.68 %
2	3.743		3.769		
3	3.776		3.819		
4	3.724		3.840		
5	3.691		3.814		
6	3.675		3.945		
7	3.583		3.765		

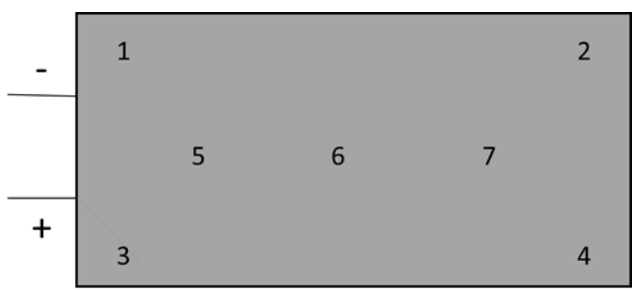

Figure 35: Regions of the pouch cell where external micrometer measurements were obtained

The external micrometer measurements indicate an overall growth of 3.68% when all regions of the cell are taken into account. This correlates to an actual change of 135 ± 50 μm. It is important to note that the cell underwent 60 symmetric charge/discharge cycles, and a longer duration of electrochemical testing may potentially lead to accelerated thickness growth upon the onset of cell failure. The pixel position vs. Δ thickness indicates a change of approximately 3.0% at a 100% SOC, and half of that upon discharge. When comparing identical states of charge, the physical micrometer measurements suggest a marginally thicker growth (3.68%) than the optical data suggests (≈1.50%). However, these measurements are well within the experimental

limitations of the reported pseudo interferometer method (± 50 μm). In summary, the reported method is a viable approach to measuring in operando swelling of lithium ion battery pouch cells, and avoiding adverse physical compression of the cell wind.

Further exploration of degradation mechanisms transitioned to the quantification of dissolved transition metals from the cathode in cycled cells as a function of time/voltage/electrolyte. These dissolved metals leach into solution at high voltage (> 4.5V), with some amount remaining dissolved in the organic electrolyte, however, the majority deposits on the anode material. The method utilized was ICP-MS to determine the concentration of dissolved metals that have deposited on the anode. **Figure 36** depicts the concentration of cobalt from tested LCO cells (4.5 and 4.6V) as a function of electrolyte composition. LCO is known to have accelerated decomposition at high voltage with Co dissolution from the cathode being a contributing factor. A baseline concentration of transition metals in the graphite anode is expected due to manufacturing processes, which is also depicted. To obtain the baseline information, a dried and untested NMC532 cell was deconstructed. A portion of the graphite anode was then digested and analyzed via ICP-MS. Although an anode portion from other untested cell chemistries (NMC622 and LCO) were not submitted for analysis, similar concentrations of transition metals (Ni, Mn, Co) are to be expected.

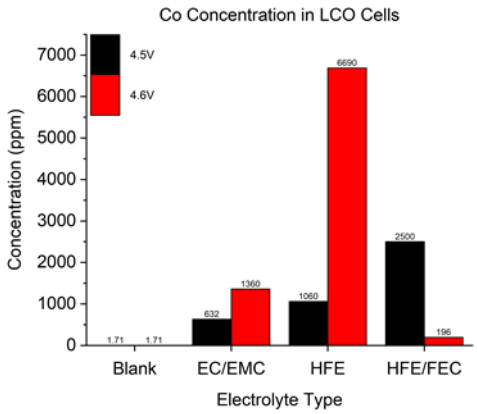

Figure 36: Dissolved Co concentrations in tested LCO cells as a function of time (200 cycles), voltage (4.5 and 4.6V), and electrolyte (EC/EMC, HFE, HFE/FEC).

Electrochemical performance data demonstrates LCO's inability to be cycled at 4.5V or above. LCO cells exhibited significant delamination of graphite from the copper current collector at both 4.5 and 4.6V, which complicated sample preparation prior to digestion. A significant amount (> 1000 ppm) of dissolved Co was detected in graphite anodes at high voltage. Dissolved Co was highest with just the fluorinated ether, and decreases upon the addition of FEC to the electrolyte (6690 vs. 196 ppm). This phenomenon is also seen in NMC532 and NMC622 cells as seen in **Figures 37** and **38**, but with a smaller effect.

Figure 37 depicts dissolved metal concentrations at the anode at both 4.2 (top row) and 4.5V (bottom row). At 4.2V, NMC532 cells have less than 100 ppm of total dissolved metals (top left), with NMC622 exhibiting a higher concentration in all electrolyte formulations (top right). Both fluorinated electrolytes contain lower amounts of all metals in both cell chemistries demonstrating the increased stability of fluorinated electrolytes over the baseline hydrocarbon

(EC/EMC) formulation. Aside from the NMC622 cell at 4.5V, cells with the HFE electrolyte contain the highest concentration of dissolved metals.

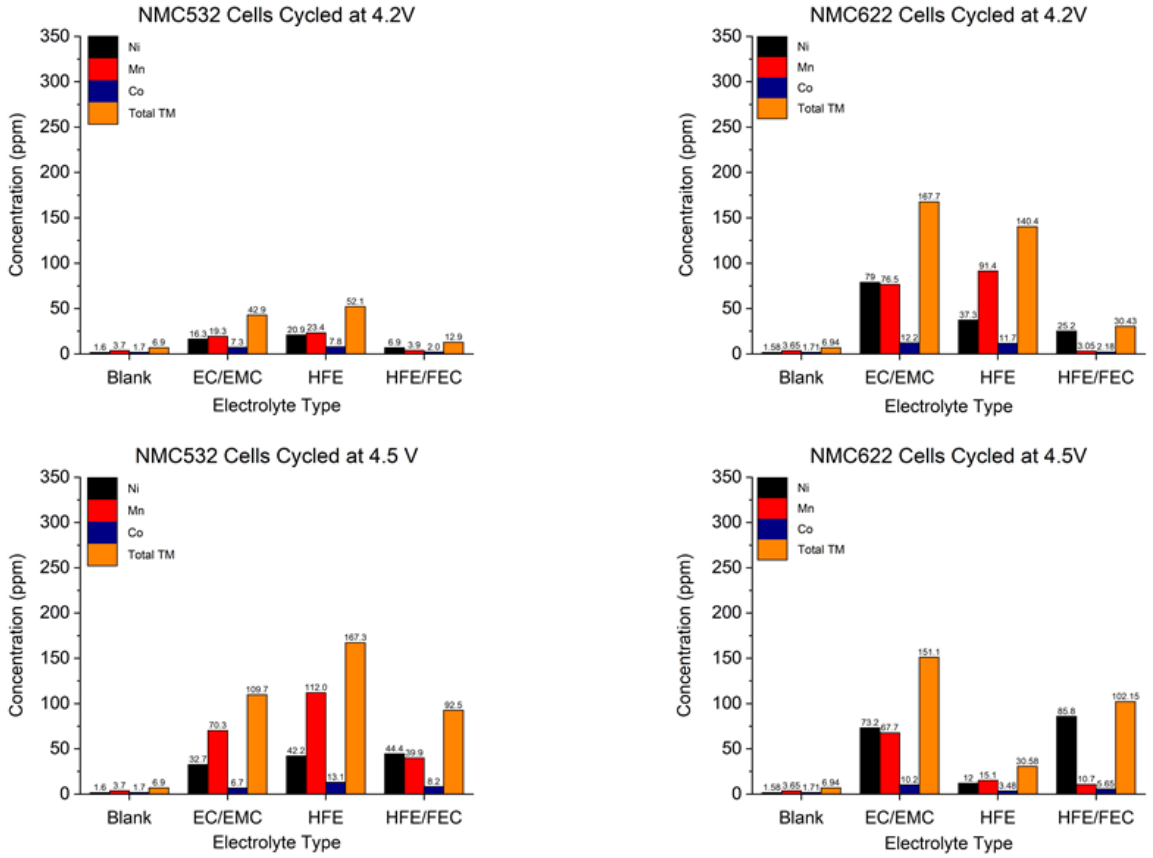

Figure 37: Dissolved metals concentration (Ni, Mn, Co) in tested NMC532 and NMC622 cells as a function of time (200 cycles), voltage (4.2 and 4.5V), and electrolyte (EC/EMC, HFE, HFE/FEC)

NMC532 cells cycled at 4.6V as a function of electrolyte are depicted in **Figure 38** (left). As seen in cells at 4.2 and 4.5V, the addition of HFE results in more dissolved metals at the anode. However, FEC suppresses the deposition of Ni, Mn, and Co. One explanation for this is that FEC could form coordination complexes with the corresponding metal, keeping it soluble in the organic solution. Its presence would not be detectible with ICP-MS of the graphite anode, but could be detected via HRESI-MS analysis of the liquid.

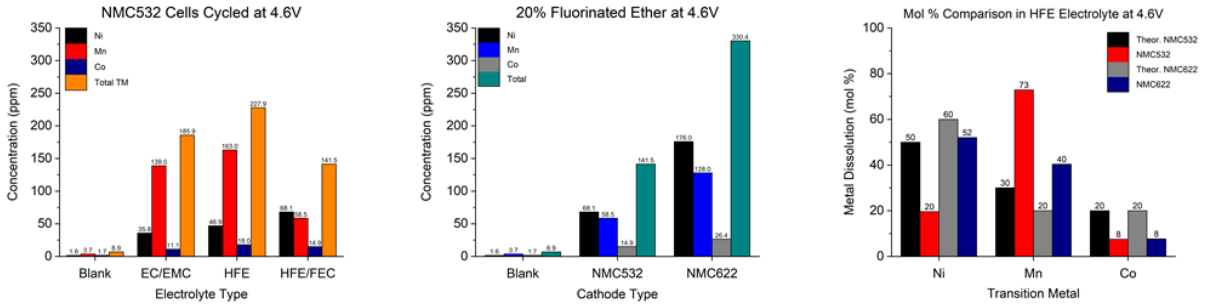

Figure 38: Dissolved metals (Ni, Mn, Co) in tested NMC532 cells at 4.6V (left). NMC532 and NMC622 cells with the HFE electrolyte at 4.6V (middle). Stoichiometric ratios of HFE cells at 4.6V post mortem versus theoretical (right)

An outstanding question targeted to resolve is whether the transition metals dissolve in a stoichiometric ratio, or if there is selective dissolution of one of the metals over the others.[24] **Figure 38** (right) depicts experimental molar ratios of dissolved metals in NMC532 (red) and NMC622 (navy) cells at 4.6V with the HFE electrolyte versus theoretical ratios (black/grey). In the NMC532 cell, the dissolution of Ni (20 %) and Co (8 %) is much lower than anticipated. Instead of being present at a 50 % mol percent as would be predicted by the stoichiometry of NMC532, Mn is present at 73 %. NMC622 exhibits similar behavior, with Ni (52 %) and Co (8 %) being present lower than stoichiometrically predicted. As seen in the NMC532 cell, Mn is also present at a higher concentration (40 %) than what would be predicted stoichiometrically.

Collaborative efforts with Dr. Julia Chan were initiated mid-project to study solid-state structural changes in high-Nickel containing cathodes as a function of electrolyte and voltage. Based on findings from dissolved metals experiments outlined in the previous section, changes to the solid-state structure of the mixed metal oxide cathode would be expected. Although it has been shown that a fluorinated electrolyte forms a protective film (CEI layer) on the surface of the cathode, it remains to be seen if this protection has any additional influence on the solid-state structure. In addition, it has also been shown that changes to structural parameters can be detected both post-mortem and *in situ* as a function of SOC.[12] The focus was on the best-performing cathode at 4.6V, NMC532 and as a function of electrolyte and SOC. Powder XRD was employed as the analytical method, with all data obtained on deconstructed cathodes post-mortem.

Powder XRD data was obtained on tested full-cells with NMC532 as the cathode (200 cycles, 0.7C, CC/CC), and analyzed delithiated at the respective upper cutoff voltage. The initial aim was to discern differences in the cathode structure from portions taken from the edge and middle areas of the cathode ribbon. Three different electrolyte formulations were investigated to probe any effects the cathode/electrolyte interphase might have on bulk property characteristics of the crystalline structure. The baseline Hydrocarbon (1.2M LiPF6, 80:20 EMC:EC + 1% PS), HFE (1.2M LiPF6, 60:20:20 EMC:HFE:EC+ 1% PS), and HFE/FEC (1.2M LiPF6, 60:20:20 EMC:HFE:FEC + 1% PS) were the formulations studied.

Localized effects on Li-ion transport kinetics could be possible contributors to observed structural changes as seen in rock salt/mixed rock salt and/or spinel phase growth,[12,14] therefore an edge versus middle portion from the cathode could exhibit these differences. **Figure 39** depicts NMC532 cathodes at 4.2V from each region of the cell.

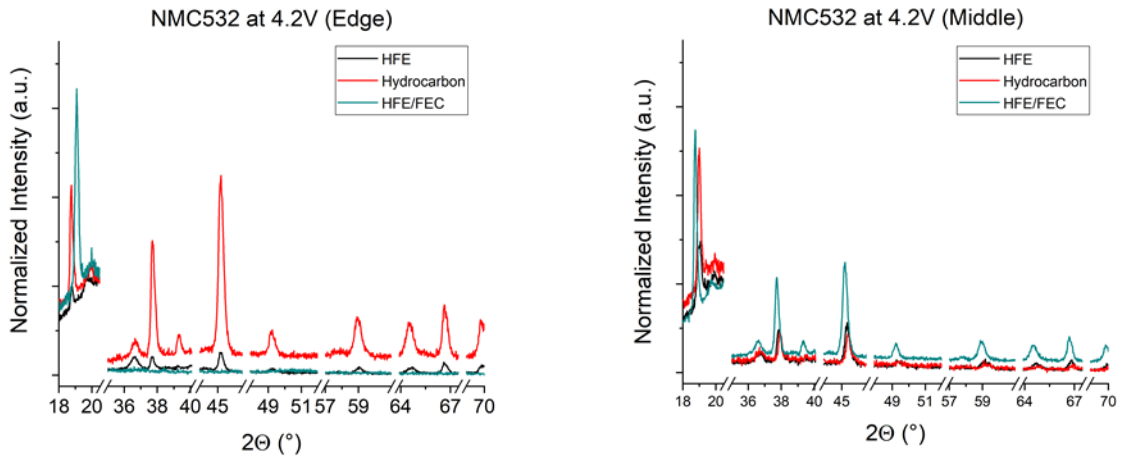

Figure 39: Edge portion of the cathode (left) and middle region of the cathode (right). Electrolyte formulation does not appear to have an effect on the bulk crystalline phase of the NMC532 material as analyzed post-mortem.

Diffraction patterns from the edge and middle portions of the NMC532 cathodes at both 4.2V and 4.6V (**Figure 40**) did not show much variance. The observed slight variations of peak location can be attributed to differing sample height. However, this could also be due to slight differing lattice parameters as a result of electrochemical testing. To probe this, it would require Reitveld refinement, which was not performed. Voltage has the largest effect on changes to the layered structure, with electrolyte composition having little to no effect.[12] Results from these measurements are consistent with previous findings in NMC cathodes.

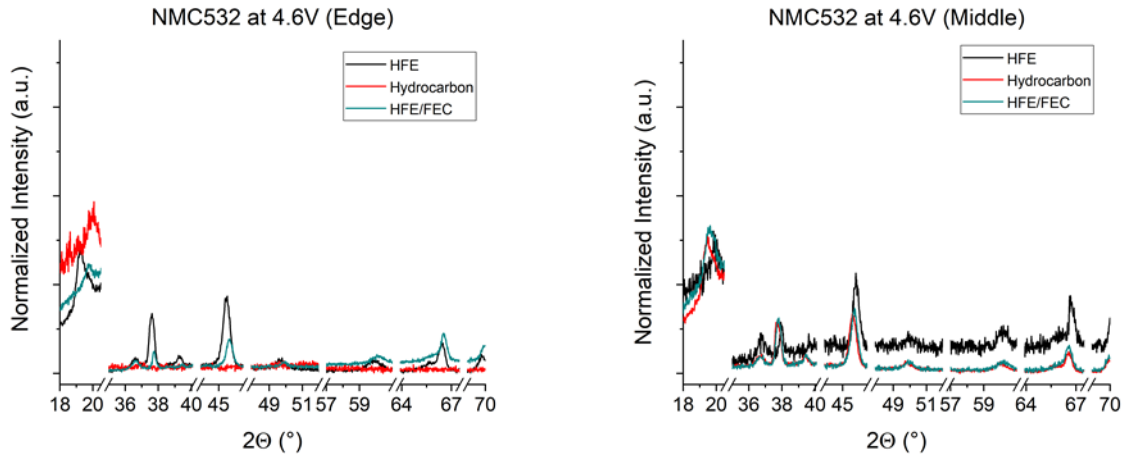

Figure 40: Edge portion of the cathode (left) and middle region of the cathode (right). As seen in the 4.2V cathode, electrolyte formulation does not appear to have an effect on the bulk crystalline phase of the NMC532 material as analyzed post-mortem.

Additional NMC532 cells were submitted to a third party analytical laboratory for analysis post-mortem. These cells were from the interim cell test batch submitted to the DOE (Idaho National Laboratory) to gauge project progression as the Go/No-Go milestone in FY2019. Four groups of NMC532 cells were submitted, of which two electrolytes were utilized. The baseline Hydrocarbon (EMC:EC), and optimized Fluorinated (EMC:FEC:HFE) formulation (1.2M LiPF6, 60:20:15:5 EMC:HFE:FEC:EC + 1% PS). Cells underwent 600 symmetric charge/discharge

cycles between either 3.0 and 4.5V or 3.0 and 4.6V, at 0.7C. Cells were deconstructed and prepared for analysis identically to those seen in **Figures 39** and **40**.

Table 3: NMC532 Cell Characteristics and OCV Prior to Disassembly

Battery Number	Electrolyte	UCV (V)	Test Voltage (V)
1	EMC:EC	4.50	4.42
2	EMC:EC	4.50	3.40
3	EMC:EC	4.60	4.48
4	EMC:EC	4.60	3.49
5	EMC:FEC:HFE	4.50	4.43
6	EMC:FEC:HFE	4.50	3.40
7	EMC:FEC:HFE	4.60	4.50
8	EMC:FEC:HFE	4.60	3.45

Diffraction patterns from these tested NMC532 cells as a function of voltage and electrolyte formulation are depicted in **Figure 41**. Cells discharged to nominally the same SOC cycled at both UCV's (Upper Cutoff Voltages) show no differences in the layered structure post-mortem.

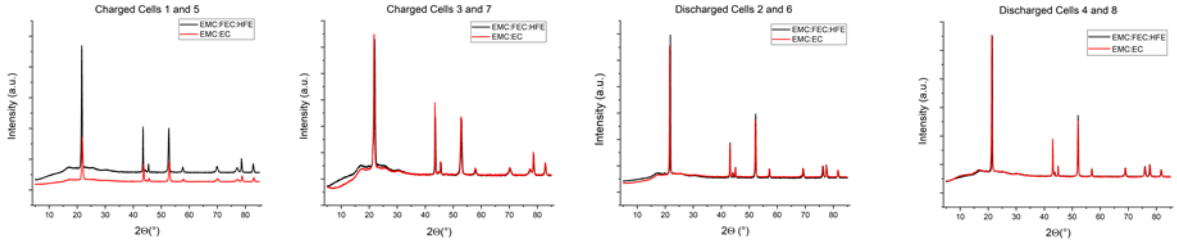

Figure 41: Charged and discharged diffraction patterns of NMC532 cathodes displayed as a function of electrolyte and voltage.

Although there was obvious cell failure at 4.6V with the EMC:EC electrolyte during interim cell analysis, it is likely not a result of cathode structure collapse. There is no difference in the bulk crystalline structure as a function of electrolyte at either voltage suggesting the driving force behind these changes cannot be altered with electrolyte formulation. **Figure 42** overlays the obtained diffraction patterns with database matches to know reference patterns of layered $Li(NiMnCo)O_2$ structures.

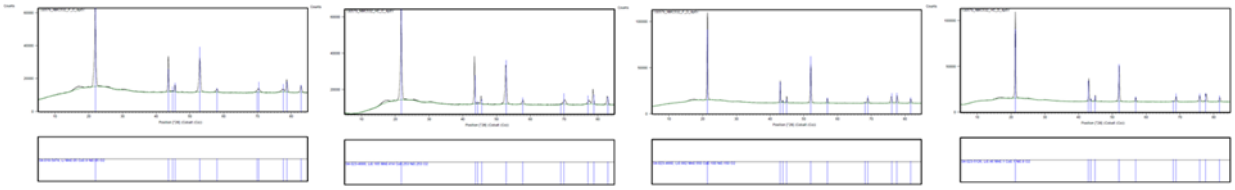

Figure 42: Reference matched diffraction patterns from charged and discharged NMC532 cathodes. Spectra are matched to the battery description outlined in **Table 3**

Discharged NMC532 cathodes do fit to a $Li_{1-x}(NiMnCo)O_2$ stoichiometry which is more lithiated than the charged cathodes. No additional bulk crystalline phases were detected in the diffraction pattern. This suggests that the interim NMC532 cells tested at INL retained their crystallinity and are good candidates for high-voltage cycling. Diffraction peak positions are shifted between all samples suggesting differences in sample heights from how the films were folded or unit cell parameter differences that may be due to stoichiometric variability between samples. No other crystalline phases were detected, and Rietveld refinement was not performed to separate these effects.

The final project deliverable was to submit cells that could meet the overall project target of at least 300 charge/discharge cycles at 4.6V. This electrochemical performance was exceeded with the submission of the interim NMC532/Graphite cells with the optimized fluorinated electrolyte formulation. **Figure 43** depicts this performance data in comparison to the identical cell chemistry with the baseline hydrocarbon electrolyte.

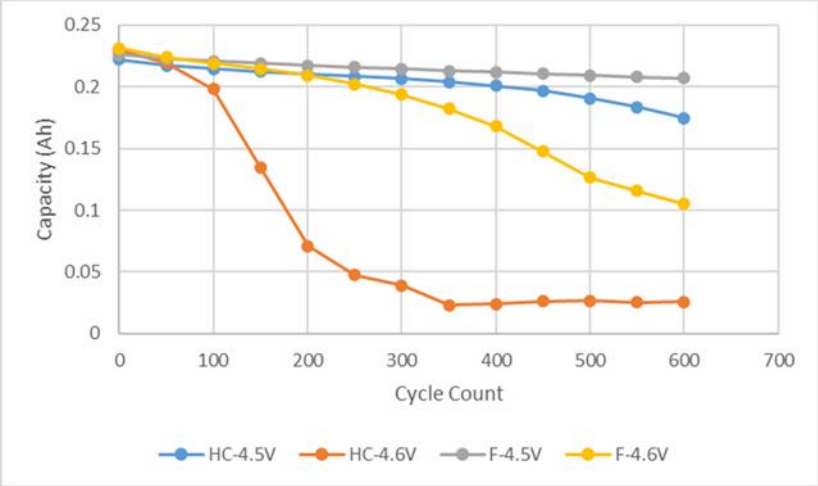

Average Capacity (RPT12)	
HC at 4.5V	0.175 ± 0.011 Ah
HC at 4.6V	0.026 ± 0.009 Ah
F at 4.5V	0.207 ± 0.002 Ah
F at 4.6V	0.105 ± 0.042 Ah

Figure 43: HC cells at 4.6V failed prematurely around cycle 150, whereas the FC cells dropped below the 80% threshold between cycles 325 and 400.

RPT12 designates the end of the test at the 600 cycle mark. HC cells cycled at 4.5 V retained 78.5% of their initial capacity, whereas HC cells at 4.6V retained almost no useable capacity at the terminus. NMC532 cells with the FC electrolyte performed significantly better than the benchmark. The optimized fluorinated electrolyte in combination with the NMC532/Graphite cell chemistry exceeded the project's target of 300 cycles at 4.6V. After 600 cycles at 4.6V, FC cells retained 45.0% of their initial capacity. FC cells cycled at 4.5V retained 90.8% of their initial capacity after 600 cycles, further demonstrating the stability of the NMC532 cathode and optimized fluorinated electrolyte at high voltage.

Final cells submitted to the DOE at the conclusion of the project were tested at both 4.4 and 4.5V. For this testing, NMC532/Graphite cells were submitted with the optimized fluorinated and baseline hydrocarbon electrolytes. Since the interim cells exceeded the overall project target, different test voltages were targeted to gauge performance. Performance above 4.5V is not demonstrated very often, therefore determining cell performance at 4.4V was desired to compare the project's performance to other projects of interest to the DOE-VTO.

After benchmarking the project's initial electrolyte formulation, insight into the role fluorinated electrolytes have in high voltage cells was obtained. Many widely known degradation mechanisms were investigated to deconvolute the role these oxidatively stable electrolyte components have:

1) While FEC is necessary to achieve electrochemical performance at high voltage, it degrades to form fluorinated gases such as fluoromethane and fluoroethane. The Daikin fluoroether is stable at 4.6V and does not gas at elevated temperatures.
2) An increased amount of FEC leads to a higher rate of gas evolution above 4.2V, especially at temperatures above ambient. High-Ni cathodes evolve gas at an increased rate at elevated temperature, with NCA gassing at the fastest rate and largest quantity.
3) Film thickness methods were developed to determine the CEI layer's thickness on NMC cathodes. Due to the three-dimensional topography of the cathode, an area averaging AES technique was implemented to measure this film thickness as a function of electrolyte. The 24-29 nm film thickness originating from the fluorinated electrolyte provides additional insight into the role fluorinated liquids play in high-voltage cells.
4) While a film also forms on cathodic surfaces when using a hydrocarbon electrolyte, its chemical composition is different from that originating from a fluorinated electrolyte. These fluorinated organic fragments on the surface supports the hypothesis that an oxidatively-resistant superficial film is formed.
5) A non-contact method for determining both reversible and irreversible cell thickness changes was developed to provide additional insight into this degradation mechanism. A 3-4 % thickness increase is seen in 4.6V NMC532/Graphite cells.
6) Transition metal dissolution of NMC cathodes was reported as a function of voltage and electrolyte, a known adverse response to high-voltage operation. NMC622 had a higher amount of dissolved metals at 4.6V when compared at NMC532 with a fluorinated electrolyte.
7) No crystalline defect phases were detected in NMC532 cells that were cycled at 4.6V. While delithiation results in crystalline phase changes in the cathode, electrolyte formulation does not appear to influence these transitions.

   NMC532/Graphite cells with the optimized fluorinated electrolyte formulation are capable of more than 300 charge/discharge cycles at 4.6V. This demonstrates the necessity of using fluorinated molecules to achieve the increased energy density needs of next-generation electric vehicles.

Cited References

1) Sunstrom, J.; Hendershot, R. E., *Daikin Advanced Lithium Ion Battery Technology – High Voltage Electrolyte – REVISED*, U.S.A., https://doi.org/10.2172/1345663

2) Xiong, D. J.; Ellis, L. D.; Petibon, R.; Hynes, T.; Liu, Q. Q.; Dahn, J. R. *J. Electrochem. Soc.*, **2017**, *164 (2)*, A340–A347
3) Streich, D.; Gueguen, A.; Mendez, M.; Chesneau, F.; Novak, P.; Berg, E. J., *J. Electrochem. Soc.*, **2016**, *163 (6)*, A964–A970

4) Xia, J.; Petibon, R.; Xiao, A.; Lamanna, W. M.; Dahn, J. R., *J. Electrochem. Soc.*, **2016**, *163 (8)*, A1637–A1645
5) Corzon S. Regino, M.; Brajter-Toth, A., *Anal. Chem.*, **1997**, *69*, 5067–5072
6) Onuki, M.; Kinoshita, S.; Sakata, Y.; Yanagidate, M.; Otake, Y.; Ue, M.; Deguchi, M., *J. Electrochem. Soc.*, **2008**, *155 (11)*, A794–A797
7) Petibon, R.; Rotermund, L.; Nelson, K. J.; Gozdz, A. S.; Dahn, J. R., *J. Electrochem. Soc.*, **2014**, *161 (6)*, A1167–A1172
8) Self, J.; Aiken, C. P.; Petibon, R.; Dahn, J. R., *J. Electrochem. Soc.*, *162 (6)*, **2015**, A796–A802
9) Igogo, T.; Sandor, D.; Mayyas, A.; Engel-Cox, J., *Supply Chain of Raw Materials Used in the Manufacturing of Light-Duty Vehicle Lithium-Ion Batteries*; NREL/TP-6A20-73374; CEMAC, August 2019
10) Buchberger, I.; Seidlmayer, S.; Pokharel, A.; Piana, M.; Hattendorff, J.; Kudejova, P.; Gilles, R.; Gasteiger, H. A., *J. Electrochem. Soc.*, **2015**, *162 (14)*, A2737-A2746
11) Li, J.; Downie, L. E.; Ma, L.; Qiu, W.; Dahn, J. R., *J. Electrochem. Soc.*, **2015**, *162 (7)*, A1401-A1408
12) Tian, C.; Hordlund, D.; Xin, H. L.; Xu, Y.; Liu, Y.; Sokaras, D.; Lin, F.; Doeff, M. M., *J. Electrochem. Soc.*, **2018**, *165 (3)*, A696-A704
13) Zhang, N.; Li, J.; Li, H.; Liu, A.; Huang, Q.; Ma, L.; Li, Y.; Dahn, J. R., *Chem. Mater.*, **2018**, *30*, 8852-8860
14) Yin, L.; Li, Z.; Mattei, G. S.; Zheng, J.; Zhao, W.; Omenya, F.; Fang, C.; Li, W.; Li, J.; Xie, Q.; Erickson, E. M.; Zhang, J.; Whittingham, M. S.; Meng, S.; Manthiram, A.; Khalifa, P. G., *Chem. Mater.*, **2020**, *32*, 1002-1010
15) Jalkanen, K.; Karppinen, J.; Skogström, L.; Laurila, T.; Nisula, M.; Vuorilehto, K., *Applied Energy*, **2015**, *154*, 160-172
16) Rasband, W. S., ImageJ, U.S. National Institutes of Health, Bethesda, MD, USA, https://imagej.nih.gov/ij/, 1997-2018
17) Qian, Y.; Niehoff, P.; Börner, M.; Grützke, M.; Mönnighoff, X.; Behrends, P.; Nowak, S.; Winter, M.; Schappacher, F. M., *J. Power Sources*, **2016**, *329*, 31-40
18) Barr, T. L.; Seal, S., *J. Vac. Sci. Technol. A*, **1995**, *13*, 1239
19) Philippe, B.; Hahlin, M.; Edström, K.; Gustafsson, T.; Siegbahn, H.; Rensmo, H., *J. Electrochem. Soc.*, **2016**, *163 (2)*, A178-A191
20) Schulz, N.; Hausbrand, R.; Dimesso, L.; Jaegermann, W., *J. Electrochem. Soc.*, **2018**, *165 (5)*, A819-A832
21) Siegel, J. B.; Stefanopulou, A. G.; Hagans, P.; Ding, Y.; Gorsich, D., *J. Electrochem. Soc.*, **2013**, *160 (8)*, A1031–A1038
22) Zhang, N.; Tang, H., *J. Power Sources*, **2012**, *218*, 52–55
23) Nagayama, M.; Ariyoshi, K.; Yamamoto, Y.; Ohzuku, T., *J. Electrochem. Soc.*, **2014**, *161 (9)*, A1388–A1393
24) Jung, R.; Linsenmann, F.; Thomas, R.; Wandt, J.; Solchenbach, S.; Maglia, F.; Stinner, C.; Tromp, M.; Gasteiger, H. A., *J. Electrochem. Soc.*, **2019**, *166 (2)*, A378-A389